JGR Atmospheres

RESEARCH ARTICLE
10.1029/2024JD041596

Modeling the Inception and Stepped Propagation of Upward Positive Lightning Leaders

John G. Pantuso[1] and **Caitano L. da Silva**[1]

[1]Department of Physics & Langmuir Lab, New Mexico Tech, Socorro, NM, USA

Key Points:

- New self-consistent leader model predicts experimentally measured leader speeds and propagation behavior
- Model postulates leader propagation in small steps and explains behavior of current measured to ground, including presence of pulses
- Criteria for upward leader ignition is strictly defined based on wire height and ambient electric field

Correspondence to:

J. G. Pantuso,
john.pantuso@student.nmt.edu

Citation:

Pantuso, J. G., & da Silva, C. L. (2024). Modeling the inception and stepped propagation of upward positive lightning leaders. *Journal of Geophysical Research: Atmospheres*, *129*, e2024JD041596. https://doi.org/10.1029/2024JD041596

Received 14 MAY 2024
Accepted 12 NOV 2024

Abstract Positive lightning leaders are a ubiquitous, yet poorly understood, component of lightning flashes. Upward lightning started by positive leaders may be formed when nearby storm activity induces electrical charges in a tall structure, such as communications towers or wind turbines. Alternatively, upward lightning can be triggered with the rocket-and-wire technique. In this paper, we introduce a new self-consistent model for this important discharge mode, one which solves Maxwell's equations under the quasi-electrostatic approximation. The model also includes a realistic treatment of the nonlinear plasma conductivity within the leader channel. This new computational tool explains the origin of the positive leader speed, of ∼10s of km/s, as well as why it displays a steady behavior over time. The model also explains the temporal evolution of current to ground measured during the early stages of rocket-triggered lightning, where the current exhibits a series of small-amplitude pulses, which disappear over time. The article also outlines straightforward criteria for leader inception, which may have practical applications for lightning protection.

Plain Language Summary Lightning which propagates upward from the ground to the cloud has been the subject of intense investigation in recent years. Upward lightning may be formed when nearby storm activity induces electrical charges in a tall structure, such as communications towers or wind turbines. Alternatively, upward lightning can be triggered with the rocket-and-wire technique, as routinely performed at New Mexico Tech's Langmuir Lab. The latter presents a great opportunity for studying the physics of lightning and its impacts. In this paper, we introduce a new self-consistent model for the initial stages of upward lightning, one rooted in basic physics laws, which describes the leader propagation as a series of small steps. The calculations explain the behavior of leader speed and current transferred to ground. A better understanding of upward lightning and its initiation and propagation could be used to better protect structures such as communication towers, tall buildings, wind turbines, or other tall structures which are prone to damage from lightning strikes.

1. Introduction

Positive upward leaders are subject of intense investigation within the field of lightning research due to their ability to damage tall structures, including radio towers, tall buildings, wind turbines, and launch vehicles. These leaders are emitted in response to sudden changes in the storm electric field due to a prior cloud-to-ground (CG) flash, or are launched upward to connect with negative stepped leaders, facilitating the attachment process (Saba et al., 2022; Schumann et al., 2019). Physical damages can happen even when CG lightning does not connect directly to the asset in question. Recently, Saba et al. (2022) reported a case where 30+ upward lightning leaders were launched toward the descending network of stepped-leader channels in a natural −CG flash. These authors reported in great detail the leader speeds and spatial scale sizes of the streamer zones involved in both polarity leaders.

Positively charged lightning leaders emanating from tall structures are by far much more common than negative ones. This is likely due to two factors: (a) the dominant cloud charge overhead is most-often of negative polarity, and (b) the stability field required to create a negative streamer zone is 2–2.5 times larger than in the positive case, as reviewed and discussed by da Silva et al. (2023). High-speed video as in Saba et al. (2022) also indicates that positive leaders are typically unbranched for many tens of meters. Upward leaders can also be generated using a rocket-and-wire triggering technique, as has been performed at the Langmuir Laboratory for Atmospheric Research at New Mexico Tech since 1979 (da Silva et al., 2023; Edens et al., 2012; Hubert et al., 1984; Idone et al., 1984; Winn et al., 2012, 2021), as well as other places around the world (Biagi et al., 2009, 2011; Lu et al., 2014, 2016; Pu et al., 2017; Qie et al., 2011, 2017; Rakov, 1998; Rakov et al., 2003). In such an experiment,

a rocket with a copper wire trailing behind is launched into the air, traveling vertically at approximately 100 m/s. The copper wire, being a good conductor, brings the ground potential hundreds of meters into the air, where upward leader emission becomes possible. Rocket-triggered lightning is particularly good at generating upward leaders, as their inception is not hindered by the production of corona, a region of ionized air which surrounds stationary, pointy, metallic objects underneath a thunderstorm. Ion corona hampers the emission of an upward leader, because it lowers the total field around the sharp tip (Aleksandrov, Bazelyan, Carpenter, et al., 2001).

In this work, we shall introduce a new model to describe the inception and propagation of upward, unbranched, positive leaders. This model adds to a wealth of previously published theoretical efforts. Existing models for leader propagation can be discriminated as 1-D versus 3-D and as electrostatic versus electrodynamic. Thus, resulting in four different classification categories: 1-D electrostatic (Aleksandrov et al., 2005; Bazelyan et al., 2008; Becerra & Cooray, 2006; Bondiou & Gallimberti, 1994; Gallimberti et al., 2002; Mazur & Ruhnke, 1998; Pasko, 2014), 3-D electrostatic (Lalande & Mazur, 2012; Mansell et al., 2002; Riousset et al., 2007), 1-D electrodynamic (Carlson et al., 2015; da Silva & Pasko, 2015), and 3-D electrodynamic (Iudin et al., 2017; Syssoev et al., 2020). Electrostatic models can be further discriminated as the ones which assume that the leader is a (nearly) perfect conductor in electrostatic equilibrium (Aleksandrov et al., 2005; Mansell et al., 2002; Mazur & Ruhnke, 1998; Pasko, 2014; Riousset et al., 2007) versus the ones where efforts are made to describe the leader temporal evolution (Aleksandrov et al., 2005; Bazelyan et al., 2008; Becerra & Cooray, 2006; Bondiou & Gallimberti, 1994; Gallimberti et al., 2002; Lalande & Mazur, 2012). The former category is based on the hypothesis of leader equipotentiality suggested by H. W. Kasemir in 1950 (Kasemir, 2013), and has been successful in explaining the bidirectional nature of lightning leaders and its consequences. The latter leverages the methodology introduced by Bondiou and Gallimberti (1994), which accounts for the fact that different leader processes have a finite time scale (corona onset, streamer-to-leader transition, leader advancement, etc.) and thus the leader temporal dynamics can be approximately tracked. This technique has been widely applied for devising onset criteria for upward leader from tall structures and lightning rods (Aleksandrov et al., 2005; Bazelyan et al., 2008).

Among these previous efforts, we would like to highlight the model developed by Becerra and Cooray (2006), which is also aimed at determining the conditions leading to initiation of a stable, upward, positive leader. Becerra and Cooray's model is focused on electrical charge, and at each step of the iteration the charge transferred to the new streamer zone is recalculated, and further propagation is only allowed if a certain threshold is surpassed. At the very beginning the charge, in the first streamer corona flash, needs to surpass 1 μC in order for a leader to emanate from the tall object's tip. After that the leader tip charge needs to surpass 65 μC/m to promote streamer-to-leader transition and continue propagating. At every step the approximate electrostatic potential distribution, modified by space charge, is used to calculate new leader properties, such as the length of new streamer zone, and advance the leader forward. More recently, Chan et al. (2018) introduced a model which contains a series of improvements with respect to Becerra and Cooray's work. Most noteworthy is the use of the charge simulation method to solve (numerically) for the charge distribution in the channel, which allows for the calculation of the exact electric field distribution ahead of the leader (to check the propagation criteria). This is an improvement with respect to the approximate expressions in Becerra and Cooray (2006). Chan et al.'s model, in a similar fashion to Gallimberti et al. (2002), includes equations to determine the: (a) relevant radial and axial length scales, which are largely determined from electrostatic considerations, and (b) leader speed, which is determined from an approximate energy conservation equation for the leader tip.

To date, there is no computational model that is capable of describing positive leader inception and propagation in a truly physics-based manner. A key issue preventing the development of such type of models is the multiscale physics involved, where leaders propagate in scales from tens of m to tens of km, but the sharpest plasma gradients need to be resolved in the 1 μm to 1 mm scale. A similar statement can also be made about temporal scales. Therefore, in this work we introduce a new model for positive lightning leaders, which presents a good compromise between fidelity to fundamental physics laws and computational efficiency. The model is rooted in Maxwell's equations and energy conservation, and at the same time it is able to simulate leader propagation for tens of meters. This is achieved by introducing a number of innovative parameterizations. This article is focused on a detailed description of this new model. A noteworthy result is that the widely observed positive leader speed, of a few tens of km/s, arises naturally from the model, and it does not need to be imposed externally. We also show how the model explains the temporal dynamics of current transferred to ground during the very early stages of rocket-triggered lightning.

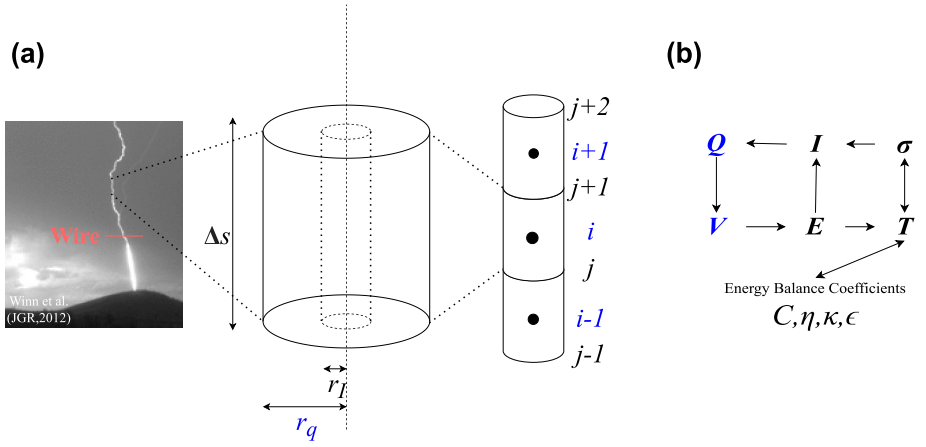

Figure 1. (a) Schematical representation of the simulation domain discretization. The wire-leader system is represented by a series of two-layered cylinders of length Δs. Charge and voltage are evaluated at the middle of the cylinders, with i indices, while all other quantities are tracked at cylinder interfaces with j indices. (b) A "formula wheel" representation of how physical quantities affect one another.

2. Model Formulation

In the subsections below we introduce a new model to describe the inception and propagation of a positive leader. For the sake of simplicity, we pick a geometry that resembles experiments performed to trigger lightning at Langmuir Lab. In this scenario a rocket brings a grounded, copper wire to a few hundred meters above ground (the rocket itself can be neglected). Thus, the first tens of meters of leader propagation, prior to when it first branches, can be modeled in one spatial dimension (height).

2.1. Model Setup and Initial Conditions

The wire-leader system is discretized into cylindrical segments. A single such segment is shown in detail in Figure 1a. An entire channel is created by stacking many of these cylinders on top of one another. Each cylinder has a length Δs and is composed of two layers: a smaller current-carrying core (radius $r_l = 1$ mm) and a larger outside sheath of charge (radius $r_q = 1$ m), a similar approach to Liang et al. (2014). Each cylindrical segment has two regions of interest where different quantities are tracked: the centers, where charge and potential are tracked, and the interfaces, where electric field, current, conductivity, temperature, and several other plasma-related quantities are tracked. Centers are indexed with i's and interfaces are indexed with j's in Figure 1a. Matching indices correspond to a cylindrical center and the *bottom* interface of that cylinder.

The wire extends up to a certain height h above the ground, of about 100–500 m. For segments within the wire r_l is set to $r_w = 0.11$ mm, which is typical for the wires used at Langmuir Lab. The radius for the second outer layer is $r_q = 1$ m, with the justification that strong radial fields and lateral ionization will spread the charge to much greater distances than r_l. The conductivity of the wire is set to 6×10^6 S/m and remained constant at all times. This value is 10% of copper's actual electrical conductivity. Justification for this value is given later in Section 4. The segments above the wire are the leader segments. All of them are given an initial conductivity of 1×10^{-12} S/m, approximately the conductivity of undisturbed air. The conductivity values of air segments are allowed to dynamically increase as streamers and leaders are formed, as discussed in detail in the subsections below. An external electric field (or ambient, E_{amb}) between 10 and 20 kV/m is applied to the system. This field corresponds to the electric field underneath a thunderstorm just prior to the rocket launch, as it is measured by a field mill sensor near the launch platform. The ambient electric field creates an ambient potential, $V_{\text{amb}} = -E_{\text{amb}}s$, where s is the vertical height above ground. The reference case in this paper is representative of successful triggers at Langmuir Lab, and it consists of a 200-m tall copper wire in a 15 kV/m electric field below a thunderstorm.

2.2. Discharge Inception

The inception of an upward positive leader starts with the emission of positive streamers from a tall, pointy structure. In a similar fashion, the successive reestablishment of a streamer zone, of about 1 m in length, is a required condition for the leader to maintain a steady propagation. The 1-m figure is cited as the minimal streamer zone size that can draw sufficient current toward the electrode, heat the air, and promote streamer-to-leader transition (Aleksandrov, Bazelyan, Carpenter, et al., 2001). Typical values reported in the literature for the threshold field required for positive streamer propagation range from 400 kV/m (Aleksandrov, Bazelyan, Carpenter, et al., 2001; Allen & Mikropoulos, 1998; Rizk, 1994) to 450 kV/m (Bazelyan & Raizer, 1998; Gallimberti, 1979), and to 500 kV/m (Becerra & Cooray, 2006; Qin & Pasko, 2014). In this work we assume that a streamer corona discharge, capable of producing a positive leader, is launched from the tip of the rocket-wire system if the electric field within 1 m exceeds the value:

$$E_{\mathrm{st}} = 400\,\delta \quad \mathrm{kVm}^{-1}, \tag{1}$$

where δ is the reduction of air density (N) in comparison to the sea-level, room-temperature value (N_0), defined as follows:

$$\delta = \frac{N(z,T)}{N_0} \simeq \delta_{\mathrm{amb}} \frac{300}{T}, \tag{2}$$

where T is the temperature in K and z is the altitude in km above mean sea level (not to be confused with the wire height above ground, h). The approximation given in Equation 2 has two terms. The first, $\delta_{\mathrm{amb}} = N_{\mathrm{amb}}/N_0 \simeq \exp(-z/9.7)$, is the reduction of air density at the altitude of interest (N_{amb}) with respect to the sea-level value, $N_0 = N(z = 0\ \mathrm{km}, T = 300\ \mathrm{K})$. At the altitude of Langmuir Lab $\delta_{\mathrm{amb}} = 0.71$. Therefore, the stability field for positive streamer propagation is reduced to 284 kV/m. The second term in the approximation in Equation 2 is the reduction of air density due to gas heating predicted by the ideal gas law.

Another widely used electric field threshold is the so-called conventional breakdown threshold, which is $E_k = 30\ \delta$ kV/cm in dry air. In electric fields higher than E_k, ionization surpasses electron attachment and conductivity grows exponentially in a gas discharge. Therefore, very close to the tip of the rocket-wire system, the field must surpass this threshold. After streamers are formed, they manage to propagate in external fields as low as $E_{\mathrm{st}} = 0.13E_k$ via a nonlinear plasma wave mechanism, which accumulates substantial charge in the streamer tip, enhancing the total electric field available for ionization. A detailed account of the streamer propagation mechanism is not the subject of this work, but it is reviewed in detail by Nijdam et al. (2020).

2.3. Electrodynamics

The model solves Maxwell's equations under the quasi-electrostatic approximation. Starting from a known charge distribution (e.g., zero charge everywhere at the beginning of the simulation), electrical charge is updated according to the continuity equation:

$$\frac{\partial \lambda}{\partial t} + \frac{\partial I}{\partial s} = 0, \tag{3}$$

where λ is the linear charge density of a channel segment, t is time, s is a linear distance along the leader (equivalent to height in this paper), and I is the current. This equation is discretized as (Luque & Ebert, 2014):

$$\frac{\partial q_i}{\partial t} = I_j - I_{j+1}, \tag{4}$$

where q_i is the total charge in a channel i-th segment and I_j is the current entering the cylindrical segment at the bottom. After the electrical charge distribution is updated, we can determine the modified electric potential:

$$V_i = V_{\text{amb},i} + \sum_m K_{im} q_m, \tag{5}$$

where V_i is the electric potential at the center of a channel segment i, K_{im} is called the kernel, and depends upon the charge geometry, and q_m is the charge in the m-th generic channel segment. The kernel used for this work is a calculation for electric potential from a charged disk, same as in Attanasio et al. (2019), with consideration for the mirror images:

$$K_{im} = \frac{1}{2\pi\epsilon_0 r_q^2}\left[\sqrt{|s_m - s_i|^2 + r_q^2} - |s_m - s_i| - \sqrt{|s_m + s_i|^2 + r_q^2} + |s_m + s_i|\right], \tag{6}$$

where s_i and s_m are the vertical heights of the i-th and m-th segments. This kernel assumes that the cylindrical segments are represented by uniformly charged disks, which is valid since $r_q > \Delta s$ where Δs is the difference between the centers of the adjacent channel segments. The time to deposit charge into the outer sheath from the inner current carrying core is about 1 μs (Liang et al., 2014). In our model, we assume that all the charge at each time instant is deposited entirely and uniformly into the sheath, and the current carrying core is emptied since our leader step interval is contrastingly much slower, on the order of tens of microseconds. Please note that Equation 6 includes the effects of image charges induced in the perfectly conducting ground underneath the simulation domain. Also note that $[K_{im}]$ is a symmetric matrix. The electric potential allows us to calculate the electric field:

$$\vec{\mathbf{E}} = -\vec{\nabla} V, \tag{7}$$

where E is the electric field and V is the electric potential. Equation 7 is discretized as follows:

$$E_j = -\frac{V_i - V_{i-1}}{\Delta s}, \tag{8}$$

where E_j is the electric field at the jth channel segment interface, V_i is the electric potential at the center of the nearby channel segments. The updated field changes the electrical current (I) according to Ohm's law:

$$I = \sigma \pi r_l^2 E, \tag{9}$$

where σ is the electrical conductivity. The updated electrical current serves as input again in the continuity equation, closing a circle that allows the model to update all electrical properties in a self-consistent manner. This circular feedback is illustrated as a formula wheel in Figure 1b (particularly the left-hand side branch). If conductivity was kept constant everywhere over time we could complete the model description right here, with Equations 3–9 being fully self-contained. In Section 2.4 we explain how conductivity evolves in the leader according to basic plasma physics principles.

2.4. Thermodynamics

A key innovation of this model is to allow for the leader conductivity to vary by more than 18 orders of magnitude in a self-consistent manner. Quantities affect one another in the way schematically shown in Figure 1b. This subsection describes the right-hand side of the formula wheel. As electrical current flows through the cylinder interfaces, Joule heating deposition transforms the air into a conducting plasma. We adapt the model developed by da Silva et al. (2019) to calculate the plasma temperature:

$$C\frac{\partial T}{\partial t} = \underbrace{\eta\sigma E^2}_{\text{Joule Heating}} - \underbrace{\frac{4\kappa}{r_l^2}(T - T_{\text{amb}})}_{\text{Radial Thermal Conduction}} + \underbrace{\kappa\frac{\partial^2 T}{\partial s^2}}_{\text{Axial Thermal Conduction}} - \underbrace{4\pi\epsilon}_{\text{Radiative Emission}}, \tag{10}$$

where the change in temperature (T) is calculated from an energy balance equation (T_{amb} = 300 K is the ambient temperature). The right-hand side of Equation 10 has four contributions, one term is for Joule heating, whereas the other three are for cooling. Equation 10 has several coefficients that describe thermodynamic and transport properties of an air plasma. All of them are given below as analytical fits to local thermodynamic equilibrium (LTE) calculations.

Heat Capacity:

$$C = 8.2 \times 10^2 \ (T/300)^{-0.5} \ \ \delta_{amb} \quad \text{J K}^{-1} \text{ m}^{-3}. \tag{11}$$

Equation 11 describes a volumetric heat capacity, precisely defined as the product of specific heat at constant pressure times mass density.

Thermal Conductivity:

$$\kappa = 6.2 \times 10^{-2} (T/300) \quad \text{W m}^{-1} \text{ K}^{-1}. \tag{12}$$

Net Radiative Emission Coefficient:

$$\epsilon = 4.0 \times 10^{11} (T/300)^{0.63} e^{-98000/T} \quad \text{W m}^{-3} \text{ sr}^{-1}, \tag{13}$$

which accounts for energy loss by the emission of electromagnetic waves in the optical portion of the spectrum. Figure 2 illustrates the dependence of these coefficients on temperature. The figure also shows comparisons between the simpler analytical fits employed here with the full LTE calculations used in da Silva et al. (2019). The fits are sufficiently accurate in the area of interest, which is around few thousands of Kelvin, and they provide reasonable agreement between the present calculations and da Silva et al. (2019). The Joule heating rate in Equation 10 also includes a parameter to describe Joule heating efficiency.

Joule Heating Efficiency:

$$\eta = \left[0.1 + 0.9 \frac{[\tanh(T/300 - 4) + 1]}{2}\right] \min\left(1, \ \frac{3E_k}{E}\right) H(t - \tau), \tag{14}$$

where η is precisely the fraction of electronic power that contributes directly to gas heating. This parameter grows nearly linearly from 10% to 100% as the temperature raises from 300 to 2000 K (da Silva et al., 2019). This functional form is assembled empirically to account for the fact that just about 10% of the electronic power, at ambient temperature, contributes directly to gas heating. Most of the remainder electron kinetic energy is transferred toward excitation of vibrational energy levels in nitrogen molecules. This is not true at higher temperatures, $\gtrsim$2000 K. The higher temperature accelerates vibrational-translational energy relaxation rates, and effectively all of the instantaneous electronic power can be transferred to gas heating (da Silva & Pasko, 2013). The field dependent term is added to account for the inefficiency of gas heating at high fields. If the field is large, above E_k, ionization will reduce the resistance (at approximate constant current) and, consequentially, reduce the Joule heating rate. We use $3E_k$ in Equation 14 to ensure this correction only applies at very high fields. The final contribution in Equation 14 involves the Heavyside function (H) and it ensures that continuous gas heating only takes place after the streamer zone is fully established, in a time scale τ. This time scale is discussed in detail below in context of Equation 15.

Changes in temperature modify the conductivity:

$$\frac{\partial \sigma}{\partial t} = -\frac{\sigma - \max(\sigma_{sz}, \sigma_{LTE})}{\tau}, \tag{15}$$

where

$$\sigma_{LTE} = 245 (T/300)^{9/8} e^{-13539/T} \quad \text{S m}^{-1}, \tag{16}$$

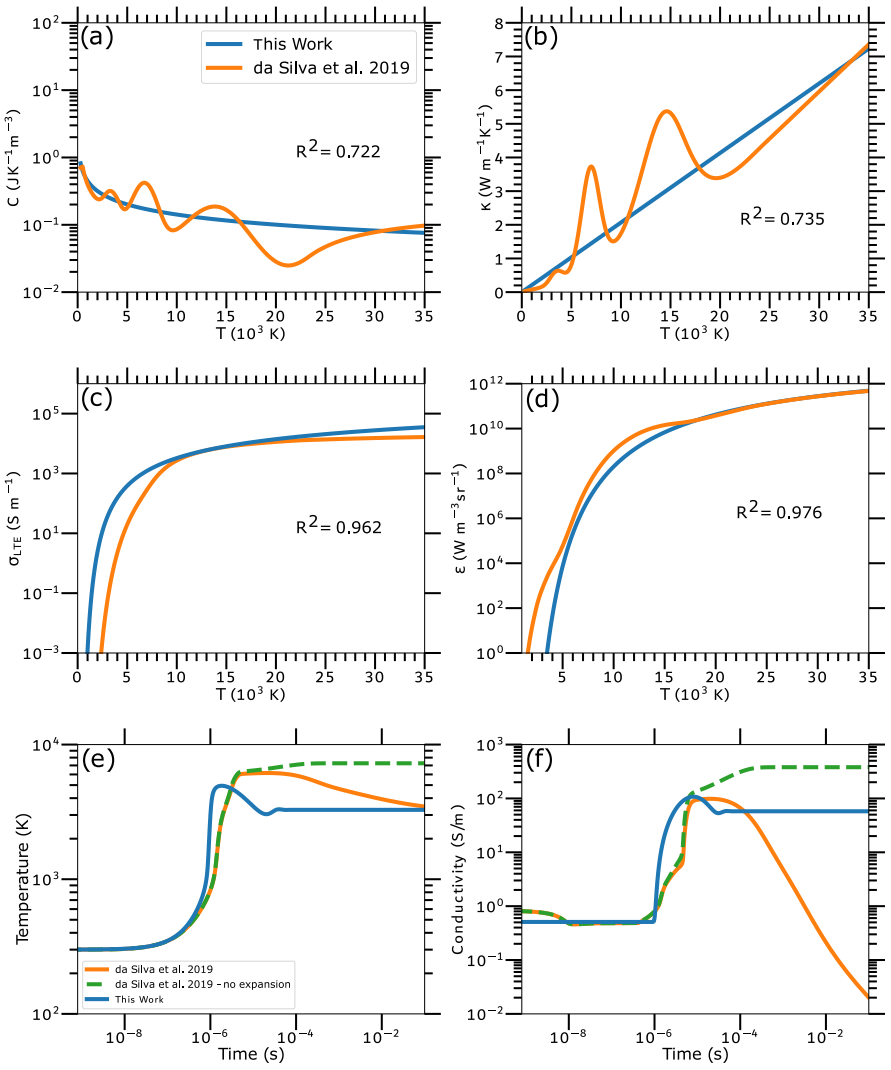

Figure 2. (a–d) Thermodynamic and transport coefficients for an equilibrium air plasma as a function of temperature: heat capacity C (a), thermal conductivity κ (b), electrical conductivity σ_{LTE} (c), and net emission coefficient ϵ (d). The four panels show the result of full thermodynamic calculations used in da Silva et al. (2019) (orange curves), and comparison to the analytical fits employed here (blue curves). Coefficients used in da Silva et al. (2019) were obtained from Boulos et al. (1994) (a–c) and Naghizadeh-Kashani et al. (2002) (d). (e–f) Comparison between simulated temperature (e) and conductivity (f) between the simplified model introduced here and previous work by da Silva et al. (2019). The latter with and without channel expansion. Simulations are performed for a current of 1 A at sea-level pressure $\delta_{\mathrm{amb}} = 1$. Initial conductivity is 0.5 S/m.

is an analytical fit for the LTE conductivity as a function of temperature (Figure 2c). Note that qualitatively, this fit has the same functional form adopted in and justified by Carlson et al. (2015). Additionally, $\sigma_{\mathrm{sz}} = 0.1$ S/m in Equation 15 is the streamer zone conductivity. The conductivity of an individual streamer is of the order of 1 S/m, as inferred from electronic density values calculated in several previous investigations (e.g., da Silva & Pasko, 2013; Liu & Pasko, 2004; Luque & Ebert, 2014). Therefore, we adopt a value that is comparable to, but lower than, the conductivity of a single streamer, to represent the volume-averaged streamer zone conductivity. In a newly created leader portion, Equation 15 describes the conductivity growth from the atmospheric value toward the streamer zone value and, therefore, τ is the time it takes to establish the streamer zone. According to Bazelyan and Raizer (2000, p. 66), this time scale can be estimated as $\tau \approx \ell_{\mathrm{sz}}/v_{\mathrm{sz}}$. Bazelyan and Raizer (2000) argue that as streamers move away from the leader tip they propagate in weaker and weaker fields and, thus, the streamer zone front has a marginal velocity, $v_{\mathrm{sz}} \approx 10^5$ m/s. In contrast, at higher fields, streamers can achieve speeds of the order of 10^6–10^7 m/s, as observed in laboratory and sprites (Briels et al., 2008; Stenbaek-Nielsen et al., 2013). For a

streamer zone length $\ell_{sz} \approx 1$ m, we obtain $\tau \approx 10$ μs. When the temperature of an existing leader segment surpasses ~2000 K, Equation 15 also describes the relaxation of the conductivity toward its equilibrium value. Aleksandrov, Bazelyan, and Konchakov (2001) demonstrated that the electron density in a leader channel at currents of a few Amperes is determined by a balance between associative ionization between nitrogen and oxygen atoms with electron-ion recombination. This equilibration of rates takes place in a time scale of ~10 μs, as also verified in subsequent works (da Silva & Pasko, 2013; Popov, 2003). Despite the fact that τ needs to describe two independent processes, in this simulation model we are able to use a single constant value to represent this quantity, $\tau = 10$ μs, because the two dissimilar processes have similar rates.

Figures 2e and 2f show a comparison between thermodynamic calculations performed with the model introduced in this section and previous work by da Silva et al. (2019). The simulation starts with a conductivity of 0.5 S/m (at sea-level pressure) and is driven by a constant current of 1 A through a single channel segment. These conditions match most closely those used in da Silva et al. (2019). Joule heating raises the temperature to several thousands of Kelvin and eventually the temperature reaches a steady-state value (Figure 2e), determined by a balance between heating and cooling in Equation 10. The temperature growth determines when the conductivity will start changing, and its steady state value is given directly from the steady-state temperature. Both this work and the 2019 model without radial expansion agree that, for a constant current, the steady state temperature and conductivity values are constant. A steady state where temperature gradually cools over time can only be achieved if radial expansion is included in the model. In this work, for the sake of simplicity, this physical process is not included in the basic equations. The justification is simple: the simulation results shown in the remainder of the paper encompass time scales of 10 μs to 0.5 ms. In these time scales, radial expansion is not quite important, and all three traces in Figures 2e and 2f agree reasonably well (within one order of magnitude).

Taylor et al. (2022) compared the effects of using different thermodynamic coefficients in the simulation of return stroke properties. Particularly, they employed the model developed by da Silva et al. (2019) and compared sets of coefficients tabulated by Boulos et al. (1994) and D'Angola et al. (2008). Taylor et al. (2022) found that the calculated return stroke temperature varied between a few to tens of percent by using the two different sets of coefficients. For this reason, we deem the agreement in Figures 2e and 2f satisfactory. In other words, if we were to employ the coefficients tabulated by D'Angola et al. (2008) in the present work, which are given as analytical expressions via truncated series of terms, we would obtain a similar order-of-magnitude agreement between the two sets of results shown in Figures 2e and 2f.

2.5. Simulating Leader Propagation

In this work we postulate that positive leaders propagate in a stepped manner, and follow to explore the consequences of such definition. Most literature concerning the physical differences between opposite-polarity leaders emphasize that negative leaders propagate in very-abrupt, VHF-noisy steps—after all this is how the Lightning Mapping Array maps negative leaders, and lightning in general. It is also stated that positive leaders propagate in a "smoother" manner, as reviewed in da Silva et al. (2023). While this statement is true, it is also vague. Evidence for the stepped propagation of positive leaders has been present in the literature for many years (Biagi et al., 2009, 2011; Huang et al., 2022; Jiang et al., 2012, 2020; Kostinskiy et al., 2016; Lu et al., 2014, 2016; Rakov et al., 2003; Wang et al., 2016, 2023; Yoshida et al., 2010). A clear example of positive-leader stepped propagation can be seen in a streak-camera record of rocket-triggered lightning collated by Rakov and Uman (2003, Figure 7.5a). Positive leader steps are brief and substantially less energetic than their opposite-polarity counterparts. Therefore, they are essentially unnoticeable. But they are key to explaining the current pulses seen at the beginning of rocket-triggered lightning flashes reported by Lu et al. (2016) and da Silva et al. (2023), as addressed later in this paper.

Saba et al. (2022) measured the length of the streamer zone in upward positive leaders emanating from residential buildings prior to the attachment of a negative cloud-to-ground lightning flash. These upward leaders took place at a mere 160–260 m away from the camera. These high-resolution measurements yielded positive streamer zone lengths, referred to in the article as corona brushes, between 0.7 and 3 m, with an average value of 1.2 m. For this reason, as well as the one provided in Section 2.2, we adopt the value $\ell_{sz} = 1$ m for the positive leader "step" length. We note that previous works, such as by Biagi et al. (2011), Jiang et al. (2012), and Wang et al. (2016), report longer streamer zone sizes. Therefore, we also explore the effects of varying ℓ_{sz} in the model-derived conclusions in Section 3.4.

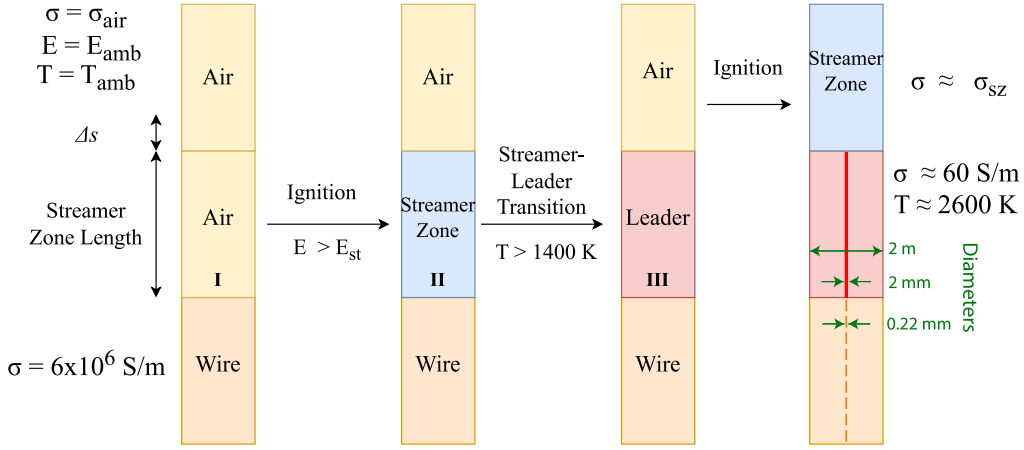

Figure 3. Illustration of the stages each computational domain segment may experience throughout its lifetime. Each block in the schematics has the size of the streamer zone and consists of several computational grid points. Stage I is undisturbed air. When the electric field reaches a critical threshold at the top of the segment, it becomes a streamer zone (stage II). Next, conductivity and temperature rise according to the energy deposition rate. Upon reaching a critical temperature, a new leader segment is created (stage III). The figure shows representative values for conductivity, electric field, and temperature in each stage.

The procedure used to simulate positive-leader inception and propagation is described in Figure 3. The simulation domain is broken down into segments of length ℓ_{sz}, each one of this consists of several grid points (e.g., 10 for $\Delta s = 10$ cm). This procedure is applied to segments above the tip of the wire; the rocket itself can be neglected. These segments can take three different forms, as shown in the figure: air (stage I, in yellow), streamer zone (stage II, in blue), and leader (stage III, in red). These segments are allowed to evolve over time into one another. Consider, for instance, what happens to the first segment, just above the wire tip, as it change stages during its life cycle.

Stage I: This is the initial stage of any segment, where the segment is essentially just an air parcel. In this stage, the conductivity and temperature are set to the ambient value in air, 1×10^{-12} S/m and 300 K.

Stage II: Whenever the electric field at the top of the segment exceeds the stability field, given in Equation 1, the segment enters stage II (first "ignition" arrow in Figure 3). A streamer zone will be established by raising the conductivity toward σ_{sz} in a time scale τ according to Equation 15. The increase in conductivity will drive current through the segment. In order for the leader to propagate a step, it is necessary that all prior Δs segments have, at some point, satisfied this electric field threshold. When looking at a diffuse arrangement of streamers which comprise the streamer zone emanating from an existing leader tip (or the wire tip), we choose *one* of these streamers to successfully become a leader, to simplify calculations and keep the model 1-D, we essentially choose the one which is pointing straight up.

Stage III: If the current is sufficient, this will heat up the streamer zone and convert it into a leader ("streamer-leader transition" arrow in Figure 3). In practice we wait for the streamer zone to be established (via the Heavyside term in Equation 14, which takes an amount of time τ), then we allow for continuous Joule heating deposition in the streamer zone. A "heating wave" ensues inside of the streamer zone, thermalizing it from the stem up, one Δs at a time. When the top of the streamer zone surpasses 1400 K, we check again if the electric field condition a distance of ℓ_{sz} ahead of the leader system satisfies the streamer zone launching condition, and if so the process is repeated and the leader continues propagating (second "ignition" arrow in Figure 3).

The streamer-to-leader transition temperature (1400 K) is defined in this model as the value at which $\sigma_{LTE} > \sigma_{sz}$. This value is approximately consistent with the number widely used in the literature, of 2000 K (Aleksandrov, Bazelyan, Carpenter, et al., 2001; da Silva & Pasko, 2013; Popov, 2003). If a streamer or streamer corona discharge is able to raise the air temperature to 1000–2000 K, it triggers a thermal-ionizational instability. This instability is characterized by an acceleration of vibrational energy relaxation rates (relaxation into translational

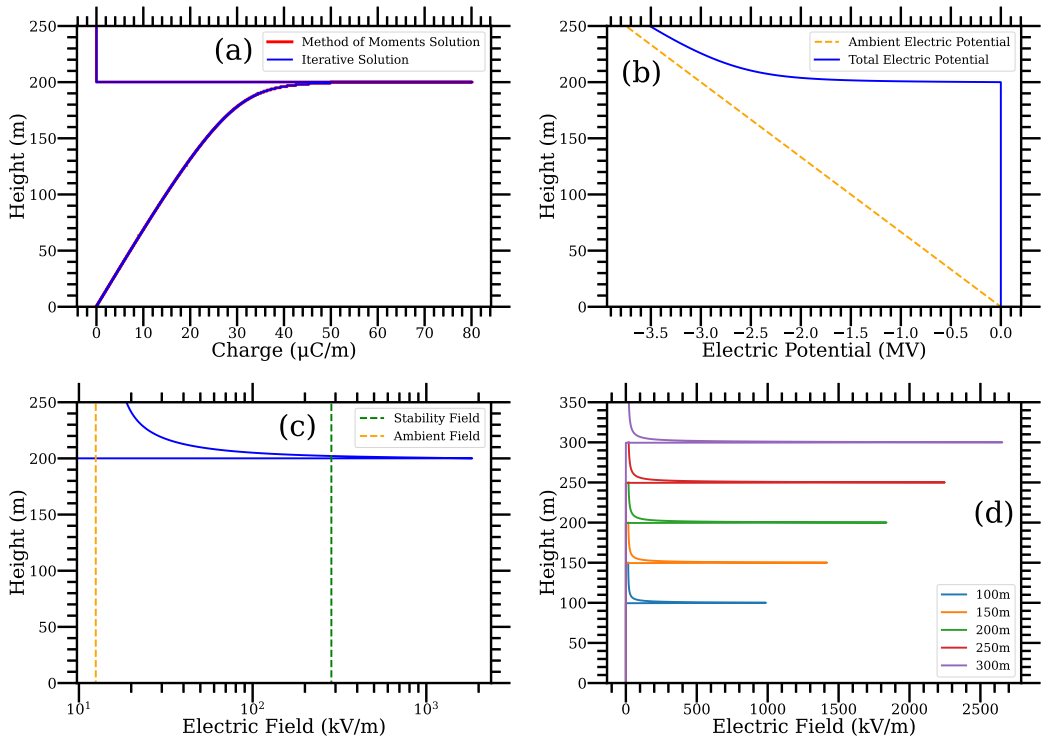

Figure 4. Electrostatic equilibrium of the rocket-wire system. (a–c) Linear charge density (a), electric potential (b), and field (c) as a function of height for $E_{amb} = 15$ kV/m and $h = 200$ m. (d) Electric field profile for cases where the rocket reaches different heights showing a linear growth of the electric field at the rocket tip as a function of h. Panel (a) demonstrates exact agreement between the iterative marching of Equation 4 toward steady state versus direct calculation with Method of Moments, Equation 18.

energy) and a change in ionization mechanism (from electron impact to thermal ionization), and as a consequence, above these temperatures transition into a leader becomes unavoidable (da Silva & Pasko, 2013, Figure 7).

2.6. Electrostatic Equilibrium

Prior to ignition of a positive leader, a rocket tethered to the ground is a system in electrostatic equilibrium, very much like a tall tower. The wire is equipotential and has the same potential as the ground, which is set at 0 V. The simulation system discussed in this work allows for a charge configuration to be utilized as an initial condition in the model. We can moderately speed up calculations by starting the simulation with the wire already in electrostatic equilibrium. The charges induced in the wire that produce such equilibrium can be determined from the electrostatic Method of Moments (Balanis, 1989, p. 674). First, we start by setting Equation 5 to zero (its known electrical potential), producing:

$$\sum_m K_{im} q_m = -V_{\text{amb,i}}. \tag{17}$$

Second, we can rewrite and rearrange the equation in matrix form as:

$$[q_m] = -[K_{im}]^{-1}[V_{\text{amb},i}], \tag{18}$$

which directly yields the charge distribution that produces zero potential everywhere inside the wire. Figure 4 shows key properties characterizing the electrostatic equilibrium achieved in the wire. Figure 4a shows the equilibrium charge distribution calculated in two ways: marching the computational model toward steady state versus a direct evaluation with Equation 18. Figures 4b and 4c show the resulting electric potential and field profiles, illustrating that the wire brings the ground potential to its tip, enhancing the field just above it.

Figures 4a–4c show calculations for a wire that is 200 m tall, under an applied field of 15 kV/m. Meanwhile, Figure 4d shows the resulting electric field for cases where the rocket-wire system attains different heights. All of these calculations can be promptly performed from the charge distribution derived via Method of Moments, without the need to run the full simulation code.

According to Bazelyan and Raizer (2000, p. 54), the amplitude of the electric field at the tip of a long rod placed in an external field (E_{amb}) is roughly approximated as $|V - V_{\text{amb}}|/r_q$, after it achieves complete electrostatic equilibrium. Since $V = 0$ for a grounded wire and V_{amb} grows linearly with height for a uniform external field (Figure 4b), the resulting electric field enhancement at the wire tip should also grow linearly with tip height (h), trending as $\propto E_{\text{amb}} h/r_q$. The effect of increase in h can be directly seen in Figure 4d.

2.7. Adjustable Model Parameters

The model has a number of parameters which can be easily adjusted. These parameters come in three distinct varieties:

1. Experimental parameters, such as wire height (h) and ambient electric field (E_{amb}), vary from one experiment to another. During a rocket-triggered lightning experiment, they cannot be controlled and, thus, result in measurement variability. Additionally, the altitude above mean sea level (δ_{amb}) at which the experiments were performed also fits this category. Model variability with experimental parameters is explored in Section 3.3.
2. Physical parameters describe a series of parameterizations of complex physical processes, which were required to be implemented in order to describe leader propagation in a computationally efficient manner. These include: the streamer zone length (ℓ_{sz}), conductivity (σ_{sz}), and establishment time scale (τ), as well as leader properties such as the current-carrying (r_l) and corona sheath (r_q) radii. Effects of key physical parameters in the simulation results are discussed in Section 3.4.
3. Numerical parameters include the spatial (Δs) and temporal (Δt) discretization steps. The wire properties (radius r_w and conductivity σ_w) in principle can be measured exactly and do not need to be listed as parameters. However, in this work we also scale σ_w down to speed up computations. Therefore, the reduced conductivity is listed here as a numerical parameter.

The reference case and most simulations in this article have $\Delta s = 10$ cm and $\Delta t = 0.2$ ns. The only time-step constraint applied is that Δt must not (substantially) exceed a modified Maxwell dielectric relaxation time scale, inferred from the model's equations to be:

$$\tau_{\text{MDR}} = \frac{\varepsilon_0}{\sigma_w}\left(\frac{r_q}{r_w}\right)^2. \tag{19}$$

It is easy to see that reducing σ_w, if at all possible, alleviates the time-step constraint and allows for faster computations. Effects of numerical parameters are discussed in Section 4.

The model is implemented with second order integration in time and first order in space. It is also worth pointing out that the model has been implemented with the capability of taking two different spatial discretization steps, one for the leader (10 cm) and another, a courser one, for the wire (taken to be 1 m everywhere in the paper).

3. Results

3.1. Criteria for Upward Leader Ignition

The discharge inception criteria adopted in this article is outlined in Section 2.2. In a nutshell, a streamer corona discharge (capable of being converted into a leader) is emitted from the rocket-wire tip if the electric field 1 m ahead of the rocket tip exceeds E_{st}, given in Equation 1. Figure 4 depicts the electrostatic scenario leading to discharge ignition. The rocket carries the wire to a certain height and brings the ground potential to that altitude. The total electric field gets substantially enhanced at the tip of the rocket due to the charges induced in the wire. As the rocket continues traveling up, it eventually reaches a height such that $E > E_{\text{st}}$ is satisfied. Another way to look into this problem is by appreciating that the electric field enhancement at the tip of the rocket-wire system increases both with wire height (h) and ambient electric field (E_{amb}), as discussed at the end of Section 2.6. We

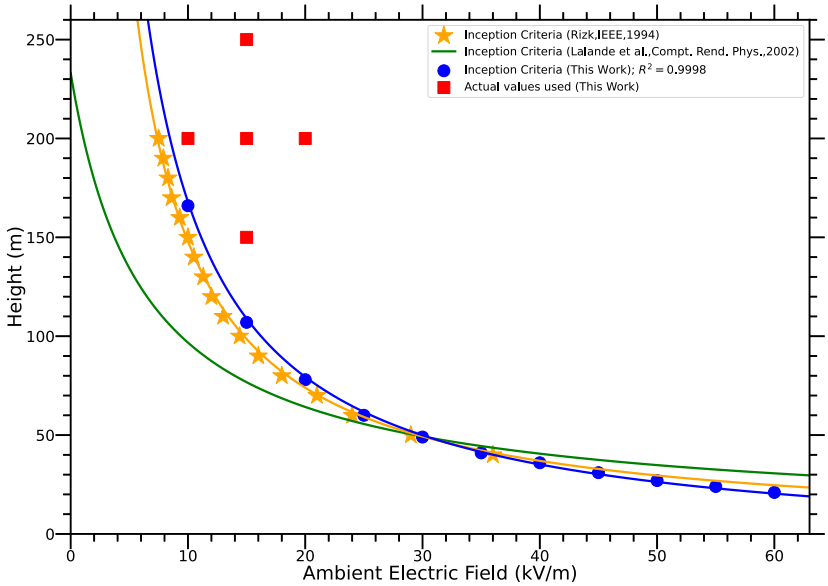

Figure 5. Threshold conditions for inception of positive leaders derived in Rizk (1994), Lalande et al. (2002), and in the present work. The curves should be read in the following manner: for a certain ambient electric field, if the rocket is able to achieve a height above the curve, a positive leader will be emitted from the rocket tip. This height can be promptly obtained from the fit Equation 20. The red squares mark actual initial conditions used in this paper. The center of the diamond corresponds to our reference case.

have repeated the calculations shown in Figure 4 for several different E_{amb} values and have determined the minimum inception height to fit the following trend:

$$h \geq \frac{1770}{E_{amb}} - 9.109, \tag{20}$$

where h is in meters and E_{amb} is in kV/m. Figure 5 shows the results of these calculations and comparison to previous estimates by Rizk (1994) and Lalande et al. (2002). All results are in fairly reasonable agreement. Calculations were performed with our model at a reduced air density of $\delta_{amb} = 0.71$. Therefore, results from the two previous investigations were scaled accordingly to the same pressure.

Note that we assume there is no corona buildup at the tip of the rocket. In rocket-triggered lightning, the ascending rocket, traveling at ~100 m/s, is able to escape any ion cloud formed around the rocket tip. This makes these estimates not suitable for determining the exact conditions necessary for initiation from a stationary object. However, it has been established that corona hampers leader initiation (Aleksandrov, Bazelyan, Carpenter, et al., 2001). Therefore, this criterion can be seen as the *minimum* requirement for initiation from any tall object.

Also shown in Figure 5, as red squares, are the actual values used in the simulations showcased in the following sections. These red squares represent typical conditions for a successful rocket-triggered lightning strike based on experience from measurements made over the years at Langmuir Lab. All cases are above the threshold inception conditions traced in the figure.

3.2. Simulation Results: The Reference Case

In this section we describe in detail a representative simulation—our reference case—which consists of a rocket raising the wire 200 m above ground in a thunderstorm field of 15 kV/m. These conditions represent well the successful triggering of lightning with the rocket-and-wire technique at Langmuir Lab ($\delta_{amb} = 0.71$), which are seldomly initiated at fields lower than 10 kV/m (Hubert et al., 1984; Winn et al., 2012), as measured by a field mill on the ground at the triggering site. The reference case also has streamer zone length, conductivity, and establishment time scale equal to 1 m, 0.1 S/m, and 10 μs, respectively. The leader has current-carrying and corona

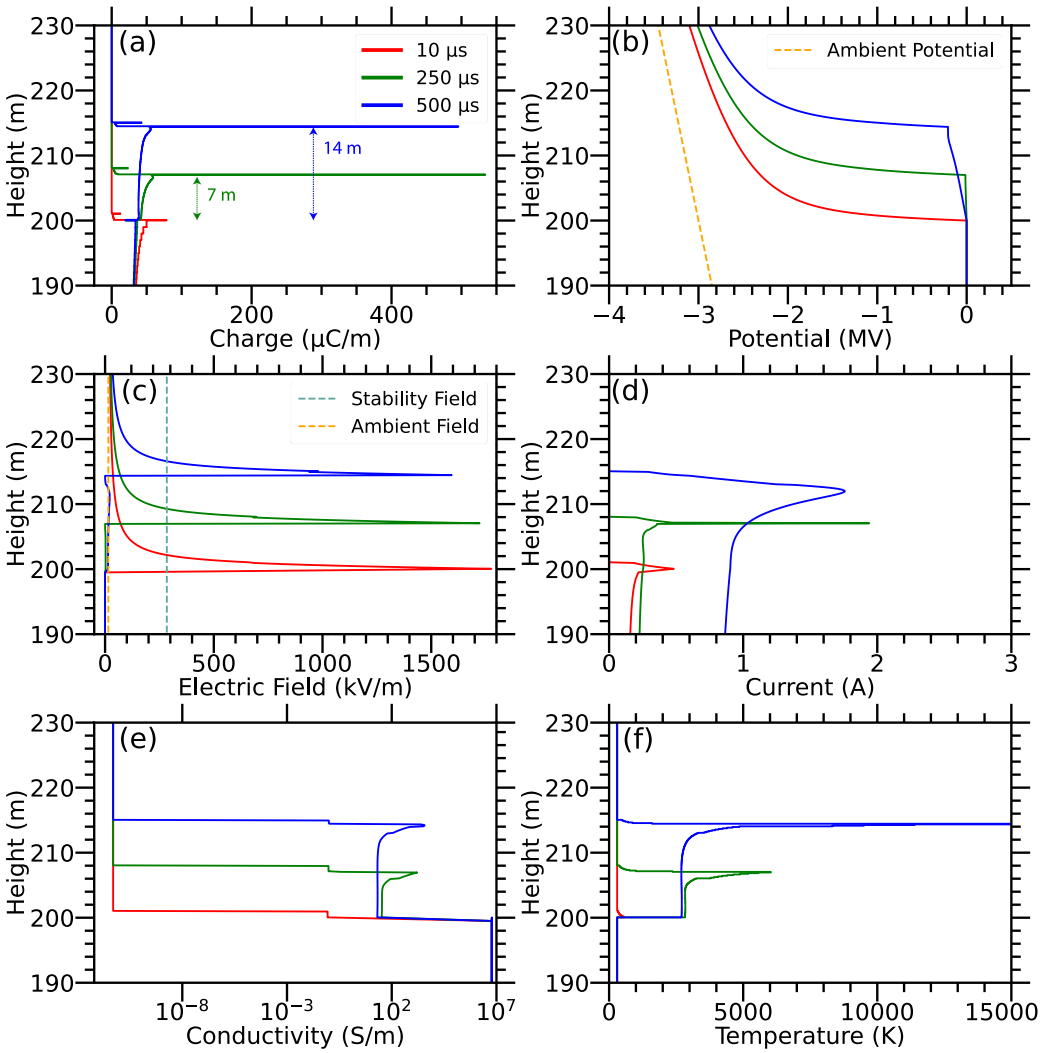

Figure 6. Vertical profiles of key leader properties: (a) linear charge density, (b) electric potential, (c) field, (d) current, (e) conductivity, and (f) temperature. The three curves in each panel show three different time instants. This simulation was performed with the reference-case driving conditions: E_{amb} = 15 kV/m and h = 200 m. In panel (a), arrows indicate the length of the fully established leader.

sheath radii equal to 1 mm and 1 m, respectively. The trailing wire has a radius and conductivity equal to 0.11 mm and 6 $\times$ 10^6 S/m (10% of copper's), respectively.

Figure 6 shows several important quantities plotted against height, for various times: linear charge density (Figure 6a), electric potential (Figure 6b), electric field (Figure 6c), current (Figure 6d), conductivity (Figure 6e), and temperature (Figure 6f). These simulations were run over the course of 500 µs, and displayed instants are 10 µs (shortly after equilibrium), 250 µs (halfway point of the simulation), and 500 µs (simulation conclusion). The leader propagates upward in time, moving up the vertical axis. Going panel by panel, Figure 6a shows the vertical distribution of charge, with two notable peaks. The most prominent peak is the existing leader tip, where a large portion of charge runs into a conductivity wall, where the conductivity drops sharply between the established hotter leader and the cooler streamer zone. The charge above this peak is the developing streamer zone, which has a less pronounced concentration at its tip.

The formation of detached, space-stem like structures in association with positive-leader streamer zones has only been observed in a limited number of studies to this date (Huang et al., 2022; Kostinskiy et al., 2016). These structures are not modeled in any way in the present work. Nonetheless, one could argue that the minor

enhancement in charge at the top of the streamer zone in Figure 6a, and subsequent minor (but still visible) disturbance in the electric field at this location in Figure 6c, could in principle create more favorable conditions for the formation of detached, space-stem like structures. Syssoev and Iudin (2023) discuss that positive leaders may, albeit rarely, produce space stems alike those more commonly observed in negative leaders by way of "floating quasi electrodes." These authors explain that the collective dynamics of streamers in the streamer zone is a key factor to produce such detached field enhancements, largely via the presence of streamers propagating nearly perpendicularly to the primary leader direction. However, they also argue that electric field enhancements, separated from the main leader tip, are substantially more frequent and intense in negative-leader streamer zones. Once again, none of these features are imposed in the present work.

Just below the streamer zone, there is a region containing the stable leader, marked with double-headed arrows in Figure 6a. The established leader has an average charge density of approximately 40–60 μC/m, just below the estimated range in previous computational investigations, which is 65–200 μC/m (Becerra & Cooray, 2006; Lalande, 1996). The electric potential (Figure 6b) moves toward zero as the wire-leader system attempts to equilibrate. The wire, a near-perfect conductor compared to the leader, maintains a potential near zero consistently. The leader struggles to equilibrate before it can propagate, creating a region of charge with linear potential drop near the leader tip (most apparent in the 500 μs snapshot). Electric potential then begins to approach the ambient potential at locations above the leader tip. The gap between the leader potential and the ambient potential is crucial to maintaining leader propagation. As such, a leader with a closing potential gap between the ambient and its own potential will eventually die.

The electric field has a notable enhancement at the leader tip, as shown in Figure 6c, many orders of magnitude greater than that of the ambient field. This field enhancement has a spatial scale of ∼10 m. There is also a faint enhancement in the electric field at the streamer zone tip, but this is oftentimes overwhelmed by the enhancement at the leader tip. The electric field inside the existing leader region approaches zero as the wire-leader system strives to reach electrostatic equilibrium. The current has a noticeable peak at the leader tip which propagates downward toward the ground (Figure 6d)—the current pulsates as the leader steps, that is, with the flashing of new streamer zones. The continuous portion of the current is only a fraction of 1 A, but the current spikes can be several Amperes in magnitude.

Perhaps the most interesting facet of the simulation results described in this section, can be seen in Figure 6e, where the vertical conductivity profile spans more than 18 orders of magnitude. From top to bottom: the air ahead of the leader, the streamer zone, the leader channel, and the wire have conductivities of 10^{-12}, 10^{-1}, $\sim 10^{2}$, and 6×10^{6} S/m, respectively. Figure 6f shows the temperature profiles, which depicts a hot leader tip with a trailing channel in approximate uniform equilibrium, determined by a balance between Joule heating and thermal conduction. This temperature profile would result in a visible leader tip, but essentially a dark trailing channel, in agreement with observations.

Figure 7 shows a zoom around the leader tip during the time interval around a leader step. The red and blue traces show two instants just prior to two sequential streamer zone emissions, while the green curve ($t = 0.26$ ms) shows an intermediate instant. Looking at either the red or blue trace, we can see the following structure: a sharp peak in charge density (Figure 7a) and temperature (Figure 7d) at the leader tip, which substantially enhances the field ahead of the leader (Figure 7b), especially within the streamer zone. The different stages of the leader, as shown in Figure 3, can be best seen in the behavior of the vertical conductivity profile. Figure 7c shows the three stages a certain portion of the computational domain above the wire may exhibit throughout its lifetime: stage I, virgin air showed as a solid line; stage II, the (1-m-long) streamer zone, shown as a dot-dashed line; and stage III, the leader, depicted as a dotted trace. In all panels the green trace depicts this intermediate instant where a thermal-ionizational wave is traversing the streamer zone. The speed of this wave, dictated by the air heating rate, is what limits the leader speed.

Figure 8 displays important quantities as a function of time. Figure 8a shows the electric field probed at three different locations. The field at the top of the streamer zone, in Figure 8a, stays well above the threshold required to propagate ($=E_{st}$), and is orders of magnitude greater than the ambient electric field. The maximum electric field is the degree of enhancement of the electric field, and it remarkably stays constant as the leader grows. This behavior is completely different from what is expected of a conductor in electrostatic equilibrium, such as the case shown in Figure 4d. All electric field traces exhibit a repeated pattern, each unit of which aligns with a one-m step

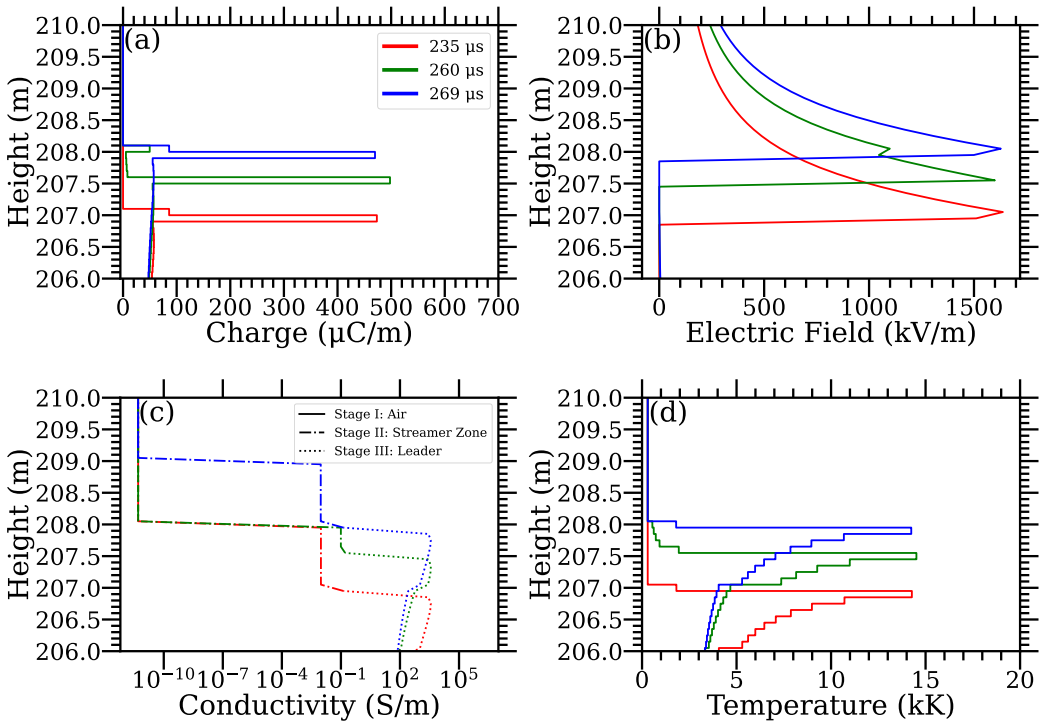

Figure 7. A zoom into the vicinity of the positive leader tip showing: (a) linear charge density, (b) electric field, (c) conductivity, and (d) temperature. The figure displays the same simulation data as in Figure 6, and in a similar format, but it shows much shorter spatial and temporal scales, just around one leader step. Panel (c) has the three stages outlined in Figure 3 plotted with different traces.

along which the leader propagates. The value of the electric field inside the leader (measured at its base, after the second step) remains less than the ambient field to ensure a sufficient voltage difference between the leader potential and ambient potential is maintained. There is a great deal of noise here due to the highly variable current (which can be seen in panel c, in orange). This noise is likely numerical noise, as the amplitude and frequency of the noise changes when the model's numerical parameters, namely Δs, are changed, but the information of the pulse packet remains the same regardless of the numerical parameters used. This numerical noise also decreases as the volatile leader tip moves farther away from the location where the electric field is measured. For more discussion on this noise and the numerical parameters of this model, see Section 4. This leader, while vigorous initially, is struggling to maintain an electric field at its base well below the ambient electric field as it propagates, implying this leader may die out after propagating a significant distance. Figure 8b shows the temperature probed at two different locations. The temperature at the leader base achieves a steady-state value close to 2500 K, which is moderately influenced by the stepped propagation. The maximum temperature anywhere is also shown. The maximum value happens around the leader tip and it oscillates with the (periodic) stepped propagation process.

Figure 8c shows the current transferred to the ground via the wire. In rocket-triggered lightning experiments, this current is measured via an in-series shunt, or via an induction coil. The yellow trace shows the direct simulation results, which are slightly contaminated by numerical dispersion, while the blue trace mimics the signal measured by an induction coil with 0.1 MHz bandwidth. This is achieved with a digital low-pass filter. Once again, in this article, we postulate that the positive leader propagates in a stepped manner. It starts with a streamer corona flash, followed by the thermalization of the streamer zone. The main consequence of this assumption is that the current to ground exhibits this pulsating waveform with each pulse corresponding to one positive leader "step." These current pulses have similar properties, namely pulse duration and interpulse interval, as the ones observed at the very early stages of rocket-triggered lightning by Lalande et al. (2002, Fig. 4), Lu et al. (2016, Fig. 1), da Silva et al. (2023, Fig. 2c), and others (Biagi et al., 2011; Wang et al., 2016). But perhaps the most noteworthy result is an explanation for why these pulses disappear over time. Detailed analysis of movie animations of the simulation data (available in the data repository (Pantuso & da Silva, 2024)) show that current pulses diminish their

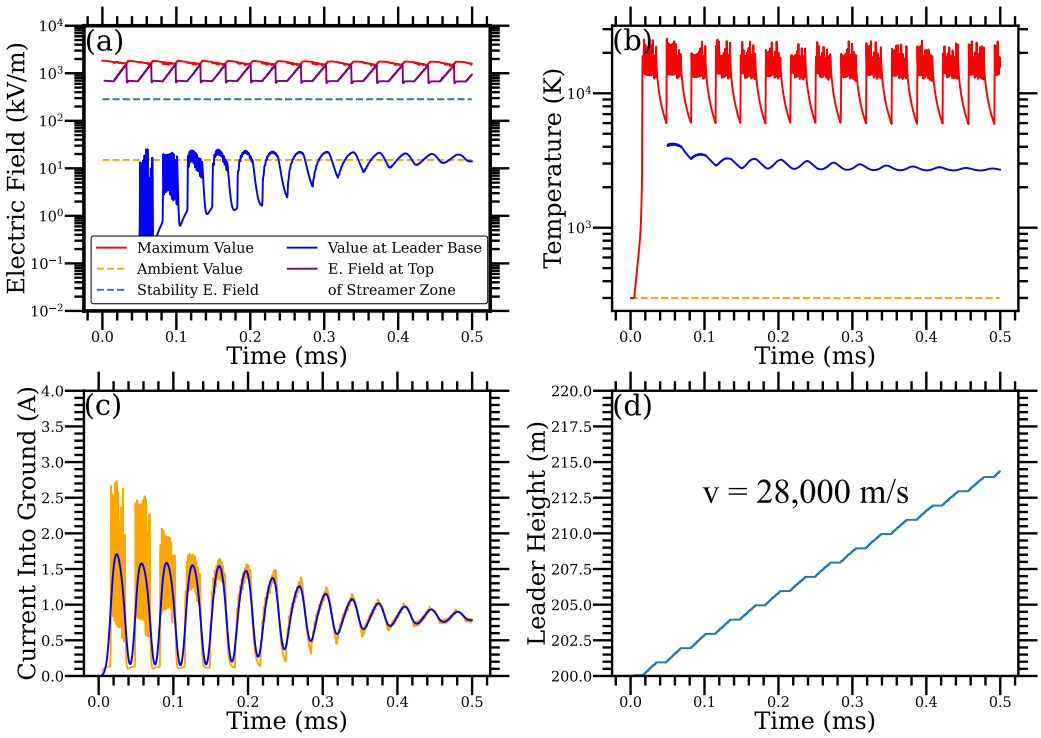

Figure 8. Temporal evolution of key leader properties: (a) electric field and (b) temperature probed at different locations (see the legend), (c) current transferred to ground via the wire, (d) and leader tip height. Panel (c) shows the current directly calculated by the model (orange trace) versus the simulated response of a measurement made with an induction coil of 0.1 MHz bandwidth (blue curve). Effects of numerical dispersion associated with the finite grid size disappear after the application of the low-pass filter.

amplitude over time because they need to travel longer and longer distances in a weekly conducting waveguide—the growing leader. This explanation is in agreement with a conjecture made by Lalande et al. (2002) and another by Jiang et al. (2012). As the pulses disappear, we can see the establishment of a nearly constant steady state current—this is the leader entering the so-called initial continuous current stage.

Finally, Figure 8d shows the leader tip position (i.e., height) versus time. The leader began at 200 m, the wire tip, and propagated 14 m in 500 μs, giving this leader an average velocity of 28,000 m/s, a quite-typical value for positive leaders. The leader tip is tracked as the highest point which exceeds 1400 K. Note that the periodic pattern of a thermalization wave in the streamer zone followed by the flashing of a new one can be easily seen in Figure 8d. However, this pattern is essentially unnoticeable in high-speed video. The entire time scale encompassed in Figure 8d corresponds to one frame of a high-speed video record made at 20,000 frames per second.

Why are positive leader speeds nearly always a few tens of km/s? This computer simulation analysis offers a straightforward answer to this question. The streamer zone is established with a speed $v_{sz} \simeq 10^5$ m/s. This speed defines $\tau = \ell_{sz}/v_{sz}$ in Equation 15. However, leader propagation is limited by how quickly the streamer zone can be heated up to several thousands of Kelvin. Let's call this time scale τ_h. Therefore, the leader speed can be approximated as $\ell_{sz}/(\tau + \tau_h)$, which is by definition a number lower than 10^5 m/s. If the two time scales are comparable, it actually cuts this figure in half. The figure 10^5 m/s should be seen as an upper limit, in conditions where the leader is overdriven by strong external fields and air heating becomes nearly instantaneous. This can happen when the electrodynamic environment is dictated by an approaching negative stepped leader during lightning attachment to grounded structures (e.g., as in Saba et al. (2022)).

Panels (c) and (d) in Figure 8, which contain information about current to ground and leader propagation, will be repeated later with a variety of differing input parameters. We will focus on these two quantities because current to ground and leader speed are accessible through measurements.

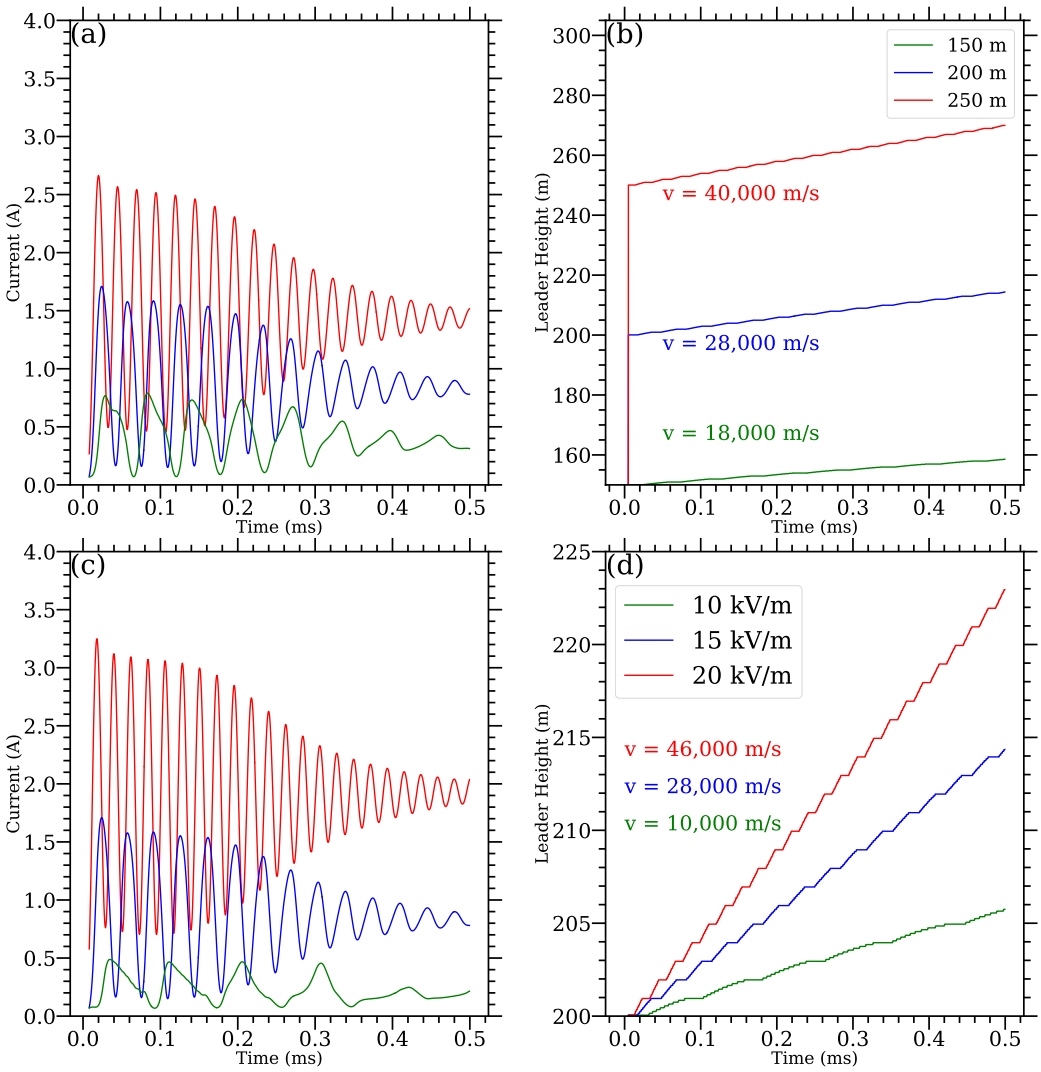

Figure 9. The effects of wire height h (a–b) and ambient electric field E_{amb} (c–d) on the current transferred to ground (a, c) and leader propagation (b, d). All parameters are identical to the reference case (15 kV/m ambient field and 200 m copper wire), with the exception of the ones listed in the legend (h and E_{amb}). The resulting leader tip speeds are also provided.

3.3. Variability With Experimental Parameters

The common procedure for triggering a lightning flash involves monitoring the electric field on the ground with a field mill sensor. The rocket is launched when field exceeds a value of the order of 10–15 kV/m, just prior to the spontaneous occurrence of a natural flash. It is likely that the field aloft is different from the one near the ground. A straightforward hypothesis is that the field should increase with proximity to the cloud base. After the rocket is launched, the height at which a leader discharge will be ignited (from the rocket tip) cannot be controlled. This variability in these two parameters can be expected to affect leader properties. Figure 9 shows the effects of wire height above ground (Figures 9a and 9b) and ambient electric field (Figures 9c and 9d), which is assumed to be uniform. It should also be noted that the fields chosen, which range from 10 to 20 kV/m, represent ambient fields on the ground representative of rocket-triggered lightning experiments performed at Langmuir Laboratory. Elevation, proximity of launch site to cloud base, humidity, and likely other factors can influence the minimum field required to initiate an upward leader. The parameter space explored in Figure 9 is the one marked with red squares in Figure 5. The blue traces in Figure 9 represent the reference case, while the green and red traces showcase the effect of parameter variation, with values listed in the figure legend. With exception of the wire

height (top row) and ambient electric field (bottom row), all other parameters are the same as in the reference case, discussed in detail in Section 3.2.

The figure shows that larger ambient electric fields produce more vigorous leaders, with larger and more-frequent current pulses, larger steady-state current, and resulting greater velocities. Note that the increase in current pulse frequency is a consequence of the faster leader speed. Varying the wire height has a similar effect on all leader properties. Both effects are similar, despite the fact that they affect the Laplacian field in different ways. (The Laplacian field is defined as the sum of the ambient field plus the field from charges induced in the wire, and it can be seen as the total external field driving leader dynamics.) An E_{amb} increase changes the Laplacian field everywhere, while an h increase only enhances the Laplacian field at the tip of the wire, as shown in Figure 4d. It is quite remarkable that despite this fundamental difference, in all cases the leader manages to achieve an approximately constant velocity. This happens because the leader strives to replicate the field enhancement at its tip. This behavior is fundamentally different than from a conductor in electrostatic equilibrium, such as shown in Figure 4d. If the leader behaved in such manner, we would see the field at its tip growing over time, and the leader would accelerate indefinitely. In agreement with observations, the model predicts that positive leader speeds should be approximately steady over time.

For the sake of clarity in Figure 9 and all subsequent figures we only show the current to ground low-pass filtered at 0.1 MHz, which mimics measurements made with an induction coil of finite bandwidth. Detailed figures and movies for these simulation cases can be found in the data repository (Pantuso & da Silva, 2024).

3.4. Effects of Parameterization of Streamer Zone Dynamics

In this section we explore the consequences of the uncertainties in the parameters introduced to parameterize the streamer zone dynamics. Figure 10 has a similar format to the preceding one, but it showcases the effects of key model parameterizations. It shows the effect of the streamer zone establishment time scale τ (Figures 10a and 10b) and the streamer zone length ℓ_{sz} (Figures 10c and 10d). All other parameters are identical to the reference case (Section 3.2). Note that $\tau = \ell_{sz}/v_{sz}$ is a function of the streamer zone length, so it is adjusted accordingly in Figures 10c and 10d. Shorter streamer zone establishment times produce, predictably, a faster leader. It is quite easy to "see" τ in Figure 10. It corresponds to the horizontal traces in panels (b) and (d), the intervals when the leader tip is "waiting" for the establishment of the new streamer zone.

Increasing the streamer zone (or step) length increases the leader speed and produces stronger pulses seen in the current-to-ground measurements. While this work is focused on the description of positive leaders. The results shown in Figures 10c and 10d may shed some light on the subject of polarity asymmetry between positive and negative leaders. The more stricter condition applied to the red traces, that is, a longer step length results into faster speed (Figure 10d) and stronger current pulses (Figure 10c). Thus, it may be that negative leaders are more impulsive (stronger current surges and VHF emissions) and faster as a consequence of their longer step lengths, of the order of a few tens of meters.

Overall, the model is stable with respect to uncertainties in the streamer zone parameterizations. A change of 50% in two key streamer zone dynamics parameters results in changes of no more than 22% in leader speed. We also note that some previous investigations have reported positive-leader streamer zones longer than 2 m (Biagi et al., 2011; Jiang et al., 2012; Wang et al., 2016) and up to 4 m in Jiang et al. (2012), for example. We have performed a simulation with a 4-m-long streamer zone (not shown) and have obtained the following two primary conclusions: (a) the leader does not start under the conditions used in Figure 10 ($E_{amb} = 15$ kV/m and $h = 200$ m), but it can be launched for higher E_{amb} or h values, and (b) the qualitative trend reported above, that speed and current pulse intensity increase with step length, remains true. The current pulses shown on the left-hand side of Figures 9 and 10 have similar duration and inter-pulse intervals to those previously reported in the literature (e.g., Biagi et al., 2011; Jiang et al., 2012, 2020), at least in order of magnitude. However, they seem to have lower amplitudes and slower risetimes than what has been reported in these previous measurements. It should be noted that this is in part due to the use of a lower electrical conductivity in the wire (10% of the copper actual conductivity), as well as due to the 0.1 MHz low-pass filter applied to the current signal to emulate an induction coil measurement.

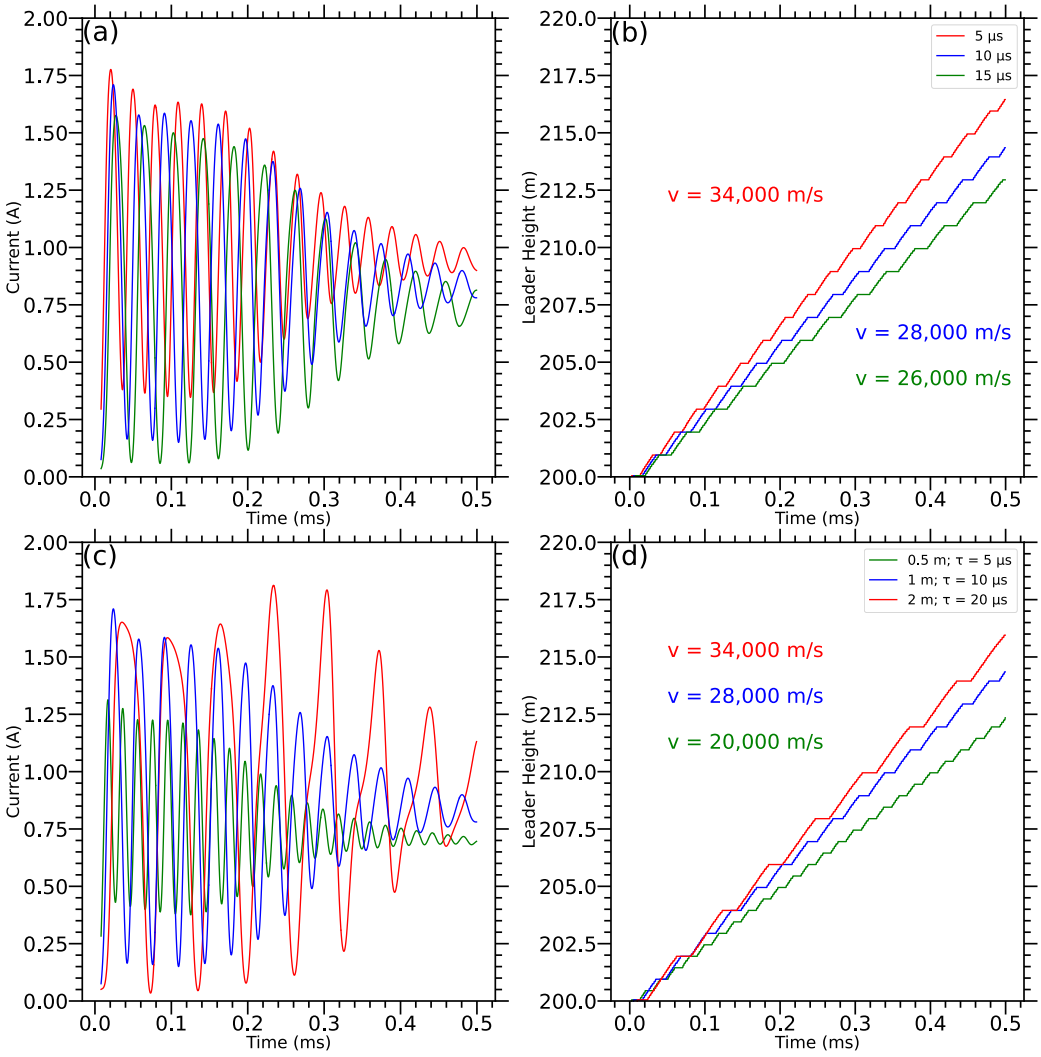

Figure 10. Effects of streamer zone establishment time scale τ (a–b) and streamer zone length ℓ_{sz} (c–d) on the current transferred to ground (a, c) and leader propagation (b, d). The time scale τ is a function of the streamer zone length, therefore streamer zone length is adjusted accordingly in panels (c) and (d). All input parameters are identical to the reference case, with the exception of the ones listed in the legend (τ and l_{sz}). The resulting leader tip speeds are also provided.

4. Discussion: Model Dependence on Numerical Parameters

Copper has a conductivity of 6×10^7 S/m. Performing simulations using the actual conductivity of copper would require a time step of approximately 0.02 ns, to ensure that Δt is not much larger than the Maxwell dielectric relaxation time constraint, given in Equation 19. While this is entirely possible, it is wholly unpractical, particular if one wishes to extend this computational model to simulate leader propagation in a flash scale. Instead, the simulation can be run using a scaled-down wire conductivity. In all simulations shown in this paper thus far, the wire conductivity was set to 6×10^6 S/m, 10% of copper's actual value. In this section, we verify that this computational simplification does not affect the analysis, except for in the case of amplitude of current to ground, which is undoubtedly affected by changes to wire conductivity. Figure 11 shows several leader properties as a function of time, including: maximum electric field (Figure 11a), temperature at leader base (Figure 11b), current to ground (Figure 11c), and leader tip height (Figure 11d). It can be seen that the value used in this article (blue trace) produces essentially identical results as a simulation with realistic wire conductivity (red trace). It is possible to reduce the conductivity even further, allowing for the increase of Δt, resulting in a speed up of the computation time. Figures 11a, 11b, and 11d show that the leader properties are essentially unchanged as the wire

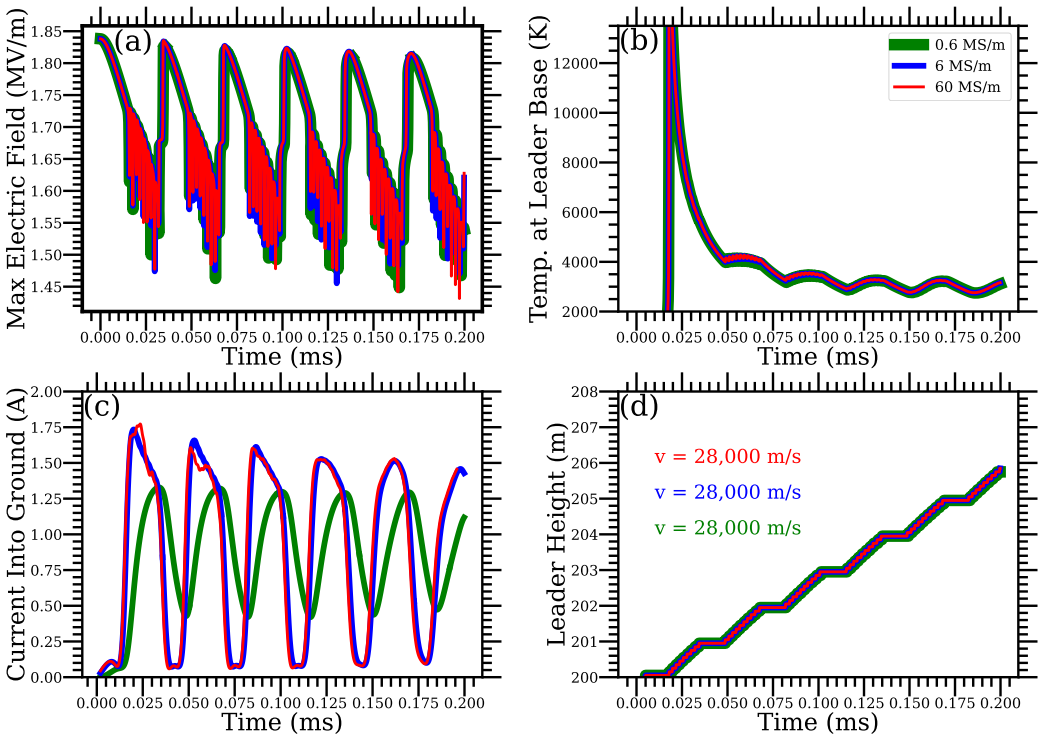

Figure 11. Effects of the wire conductivity on the (a) maximum electric field, (b) temperature at leader base, (c) current transferred to ground, and (d) leader propagation. All input parameters are identical to the reference case, with the exception of the ones listed in the legend plus the time step for the realistic copper conductivity case, which is set to $\Delta t = 0.02$ ns to satisfy the Maxwell dielectric relaxation condition.

conductivity is further reduced to 6×10^5 S/m. This remains true as long as the wire conductivity is much larger than the leader conductivity (let's say two orders of magnitude larger). However, the waveshape of the current transferred to ground is directly affected by the wire conductivity. A lower conductivity increases attenuation and dispersion, distorting the current pulses, as it can be seen in Figure 11c. An interesting consequence of this analysis is that, if one only cares about the positive-leader properties, the wire conductivity can be set as low as 10^4-10^5 S/m without any loss of information. This can speed computations by two or three orders of magnitude!

Similarly to any other model which involves spatiotemporal dynamics, the one introduced in this paper has two standard numerical parameters which describe the discretization of the otherwise continuous time and space. The effects resulting from changing these numerical parameters on the simulated leader can be seen in Figure 12. Space is discretized into small Δs-sized pieces, as seen in Figure 1. Higher precision spatial definition is a superior option, but not readily computationally practical, particularly when combined with a high-precision temporal resolution. In compromise, the bulk of simulations in this work were run with a 10-cm spatial resolution, allowing for 10 grid points within the streamer zone. Figures 12a and 12b show that the simulation results are reasonably stable regarding changes in Δs. Particularly, it shows that the 10-cm value chosen compares quite well with results obtained with finer resolution (5 cm). The misalignment of pulses in Figure 12a is a result of the slightly different leader speeds.

The simulation is even more resilient to changes in temporal resolution, likely due to the already strict time step ceiling imposed by the Maxwell dielectric relaxation time constraint, which for the parameters used is ~0.2 ns. Figures 12c and 12d show that there is no difference between the reference case simulations and one with a ten-fold finer temporal resolution. The case with coarser temporal resolution needs to be discussed with more care. Since 1 ns is longer than the Maxwell dielectric relaxation time scale, the only way the simulation can be performed is if we further reduce the wire conductivity. The key consequence is that the leader properties are essentially the same in comparison to the reference case, including its propagation (Figure 12d), but the current pulses observed at ground level are attenuated, for the same reasons as in Figure 11c.

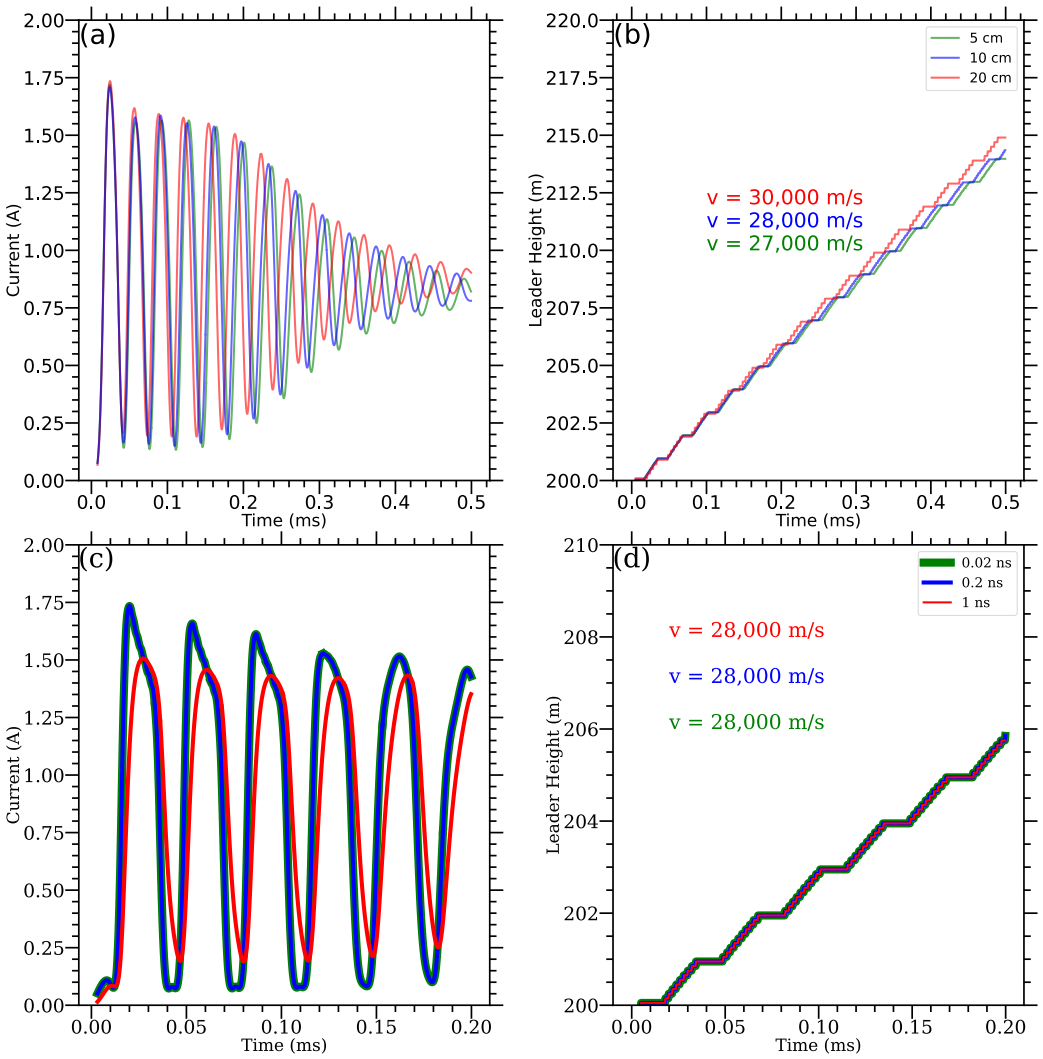

Figure 12. Effects of spatial (a–b) and temporal (c–d) discretization on the current transferred to ground (a, c) and leader propagation (b, d). All input parameters are identical to the reference case, with the exception of the ones listed in the legend as well as wire conductivity (Δs, Δt, and σ_w). The wire conductivity σ_w for the $\Delta t = 1$ ns simulation is set to 1.2×10^6 S/m to satisfy the Maxwell dielectric relaxation condition. The resulting leader tip speeds are also provided.

5. Conclusions

In this work we introduced a novel computer model to simulate the inception and propagation of positive lightning leaders. It presents a self-consistent solution to the plasma-electrodynamic problem under the quasi-electrostatic approximation. The model tackles the problem's inherent complexity by introducing a series of parameterizations to both reduce the 3-D problem into one dimension, and also to describe the intricate multiscale streamer zone dynamics through just three parameters. The model predicts physically sound values for currents, charge densities, temperature, speed, and more. A key innovation introduced in this work is the inclusion of a self-consistent evaluation of the plasma conductivity, from a solution to the energy conservation equation.

We have shown in this work that our model replicates ignition criteria similar to those previously proposed in the literature. But beyond simple leader inception criteria for rocket-triggered lightning, this computer simulation tool can be run on a need-basis to determine if a full-fledged leader (referred to as viable) should develop for particular sets of experimental conditions and geometries.

We have also shown how the current pulses at the early stages of rocket-triggered lightning can be explained as resulting from 1-m-long leader steps. These steps involve the flashing of a streamer corona discharge (the streamer zone) followed by its thermalization, and thus are fundamentally different than steps in negative leaders, especially in scale. In all of the 13 different simulation runs showcased in this paper, the positive leader achieves an approximately steady velocity, ranging between 10 and 46 km/s for different applied electric fields. A detailed analysis of the model's parameter space has shown that the intensity of current transferred to ground, and its superposed pulses, as well as leader speed, increase with ambient electric field, wire height, and (imposed) streamer zone length.

The model is built with simplicity, efficiency, and pliability in mind, and is thus ready to be expanded upon. In the future, we hope to use this system of coupled thermodynamic and electrodynamic equations to model leaders in different types of flashes, as well as to extend it to account for other leader variants, including negative, bidirectional, space, and dart leaders. The fact that this model provides leader temperature opens up an entire avenue for calculation of optical emissions and chemical impacts. This shall be the subject of future research.

Data Availability Statement

Simulation data used in this publication is available online (Pantuso & da Silva, 2024). The data repository contains detailed figures for all simulation cases shown in this paper, in the style of Figures 6 and 8. It also contains movie animations for the five simulation cases marked in Figure 5.

Acknowledgments
This work has been supported by NSF CAREER award AGS-2046043 to New Mexico Tech.

References

Aleksandrov, N. L., Bazelyan, E. M., Carpenter, R. B., Jr., Drabkin, M. M., & Raizer, Y. P. (2001). The effect of coronae on leader initiation and development under thunderstorm conditions in long air gaps. *Journal of Physics D: Applied Physics*, *34*(22), 3256–3266. https://doi.org/10.1088/0022-3727/34/22/309

Aleksandrov, N. L., Bazelyan, E. M., D'Alessandro, F., & Raizer, Y. P. (2005). Dependence of lightning rod efficacy on its geometric dimensions – A computer simulation. *Journal of Physics D Applied Physics*, *38*(8), 1225–1238. https://doi.org/10.1088/0022-3727/38/8/021

Aleksandrov, N. L., Bazelyan, E. M., & Konchakov, A. M. (2001). Plasma parameters in the channel of a long leader in air. *Plasma Physics Reports*, *27*(10), 875–885. https://doi.org/10.1134/1.1409721

Allen, N. L., & Mikropoulos, P. N. (1998). Dynamics of streamer propagation in air. *Journal of Physics D: Applied Physics*, *32*(8), 913–919. https://doi.org/10.1088/0022-3727/32/8/012

Attanasio, A., Krehbiel, P. R., & da Silva, C. L. (2019). Griffiths and Phelps lightning initiation model, revisited. *Journal of Geophysical Research: Atmospheres*, *124*(14), 8076–8094. https://doi.org/10.1029/2019JD030399

Balanis, C. A. (1989). *Advanced engineering electromagnetics*. John Wiley & Sons, Inc.

Bazelyan, E. M., & Raizer, Y. (1998). *Spark discharge*. CRC Press.

Bazelyan, E. M., & Raizer, Y. P. (2000). *Lightning physics and lightning protection*. Institute of Physics Publishing.

Bazelyan, E. M., Raizer, Y. P., & Aleksandrov, N. L. (2008). Corona initiated from grounded objects under thunderstorm conditions and its influence on lightning attachment. *Plasma Sources Science and Technology*, *17*(2), 024015. https://doi.org/10.1088/0963-0252/17/2/024015

Becerra, M., & Cooray, V. (2006). A self-consistent upward leader propagation model. *Journal of Physics D: Applied Physics*, *39*(16), 3708–3715. https://doi.org/10.1088/0022-3727/39/16/028

Biagi, C. J., Jordan, D. M., Uman, M. A., Hill, J. D., Beasley, W. H., & Howard, J. (2009). High-speed video observations of rocket-and-wire initiated lightning. *Geophysical Research Letters*, *36*(15), L15801. https://doi.org/10.1029/2009GL038525

Biagi, C. J., Uman, M. A., Hill, J. D., & Jordan, D. M. (2011). Observations of the initial, upward-propagating, positive leader steps in a rocket-and-wire triggered lightning discharge. *Geophysical Research Letters*, *38*(24), L24809. https://doi.org/10.1029/2011GL049944

Bondiou, A., & Gallimberti, I. (1994). Theoretical modeling of the development of the positive spark in long air gaps. *Journal of Physics D: Applied Physics*, *27*(6), 1252–1266. https://doi.org/10.1088/0022-3727/27/6/024

Boulos, M. I., Fauchais, P., & Pfender, E. (1994). *Thermal plasmas, fundamentals and applications* (Vol. 1). Plenum.

Briels, T. M. P., Kos, J., Winands, G. J. J., van Veldhuizen, E. M., & Ebert, U. (2008). Positive and negative streamers in ambient air: Measuring diameter, velocity and dissipated energy. *Journal of Physics D: Applied Physics*, *41*(23), 234004. https://doi.org/10.1088/0022-3727/41/23/234004

Carlson, B. E., Liang, C., Bitzer, P., & Christian, H. (2015). Time domain simulations of preliminary breakdown pulses in natural lightning. *Journal of Geophysical Research: Atmospheres*, *120*(11), 5316–5333. https://doi.org/10.1002/2014JD022765

Chan, M.-K., Chen, M., & ping Du, Y. (2018). A macroscopic physical model for self-initiated upward leaders from tall grounded objects and its application. *Atmospheric Research*, *200*, 13–24. https://doi.org/10.1016/j.atmosres.2017.09.012

D'Angola, A., Colonna, G., Gorse, C., & Capitelli, M. (2008). Thermodynamic and transport properties in equilibrium air plasmas in a wide pressure and temperature range. *European Physical Journal D: Atomic, Molecular and Optical Physics*, *46*(1), 129–150. https://doi.org/10.1140/epjd/e2007-00305-4

da Silva, C. L., & Pasko, V. P. (2013). Dynamics of streamer-to-leader transition at reduced air densities and its implications for propagation of lightning leaders and gigantic jets. *Journal of Geophysical Research: Atmospheres*, *118*(24), 13561–13590. https://doi.org/10.1002/2013jd020618

da Silva, C. L., & Pasko, V. P. (2015). Physical mechanism of initial breakdown pulses and narrow bipolar events in lightning discharges. *Journal of Geophysical Research: Atmospheres*, *120*(10), 4989–5009. https://doi.org/10.1002/2015JD023209

da Silva, C. L., Sonnenfeld, R. G., Edens, H. E., Krehbiel, P. R., Quick, M., & Koshak, W. (2019). The plasma nature of lightning channels and the resulting nonlinear resistance. *Journal of Geophysical Research: Atmospheres*, *124*(16), 9442–9463. https://doi.org/10.1029/2019JD030693

da Silva, C. L., Winn, W. P., Taylor, M. C., Aulich, G. D., Hunyady, S. J., Eack, K. B., et al. (2023). Polarity asymmetries in rocket-triggered lightning. *Geophysical Research Letters*, *50*(17), e2023GL105041. https://doi.org/10.1029/2023GL105041

Edens, H. E., Eack, K. B., Eastvedt, E. M., Trueblood, J. J., Winn, W. P., Krehbiel, P. R., et al. (2012). VHF lightning mapping observations of a triggered lightning flash. *Geophysical Research Letters*, *39*(19), L19807. https://doi.org/10.1029/2012GL053666

Gallimberti, I. (1979). The mechanism of the long spark formation. *Journal de Physique Colloques*, *40*(C7), 193–250. https://doi.org/10.1051/jphyscol:19797440

Gallimberti, I., Bacchiega, G., Bondiou-Clergerie, A., & Lalande, P. (2002). Fundamental processes in long air gap discharges. *Comptes Rendus Physique*, *3*(10), 1335–1359. https://doi.org/10.1016/S1631-0705(02)01414-7

Huang, S., Chen, W., Fu, Z., Fu, Y., Xiang, N., Qiu, X., et al. (2022). Separate luminous structures leading positive leader steps. *Nature Communications*, *14*(1), 3655. https://doi.org/10.1038/s41467-022-31409-x

Hubert, P., Laroche, P., Eybert-Berard, A., & Barret, L. (1984). Triggered lightning in New Mexico. *Journal of Geophysical Research*, *89*(D2), 2511–2521. https://doi.org/10.1029/jd089id02p02511

Idone, V. P., Orville, R. E., Hubert, P., Barret, L., & Eybert-Berard, A. (1984). Correlated observations of three triggered lightning flashes. *Journal of Geophysical Research*, *89*(D1), 1385–1394. https://doi.org/10.1029/JD089iD01p01385

Iudin, D. I., Rakov, V. A., Mareev, E. A., Iudin, F. D., Syssoev, A., & Davydenko, S. (2017). Advanced numerical model of lightning development: Application to studying the role of LPCR in determining lightning type. *Journal of Geophysical Research: Atmospheres*, *122*(12), 6416–6430. https://doi.org/10.1002/2016JD026261

Jiang, R., Qie, X., Li, Z., Zhang, H., Li, X., Yuan, S., et al. (2020). Luminous crown residual vs. bright space segment: Characteristical structures for the intermittent positive and negative leaders of triggered lightning. *Geophysical Research Letters*, *47*(21), e2020GL088107. https://doi.org/10.1029/2020GL088107

Jiang, R., Qie, X., Wang, C., & Yang, J. (2012). Propagating features of upward positive leaders in the initial stage of rocket-triggered lightning. *Atmospheric Research*, *129–130*, 90–96. https://doi.org/10.1016/j.atmosres.2012.09.005

Kasemir, H. W. (2013). Qualitative overview of potential, field and charge conditions in the case of a lightning discharge in the storm cloud. In V. Mazur & L. H. Ruhnke (Eds.), *Heinz-Wolfram Kasemir: His Collected Works* (pp. 398–411). American Geophysical Union. https://doi.org/10.1002/9781118704813.ch27

Kostinskiy, A. Y., Syssoev, V. S., Bogatov, N. A., Mareev, E. A., Andreev, M. G., Bulatov, M. U., et al. (2016). Abrupt elongation (stepping) of negative and positive leaders culminating in an intense corona streamer burst: Observations in long sparks and implications for lightning. *Journal of Geophysical Research: Atmospheres*, *123*(10), 5360–5375. https://doi.org/10.1029/2017JD027997

Lalande, P. (1996). *Study of the lightning stroke conditions on a grounded structure* (Doctoral Thesis).A Publication of Office National d'Etudes et de Recherches A'erospatiales.

Lalande, P., Bondiou-Clergerie, A., Bacchiege, G., & Gallimberti, I. (2002). Observations and modeling of lightning leaders. *Comptes Rendus Physique*, *3*(10), 1375–1392. https://doi.org/10.1016/s1631-0705(02)01413-5

Lalande, P., & Mazur, V. (2012). A physical model of branching in upward leaders. *Aerospace Lab Journal*, *5*.

Liang, C., Carlson, B., Lehtinen, N., Cohen, M., Marshall, R. A., & Inan, U. S. (2014). Differing current and optical return stroke speeds in lightning. *Geophysical Research Letters*, *41*(7), 2561–2567. https://doi.org/10.1002/2014GL059703

Liu, N. Y., & Pasko, V. P. (2004). Effects of photoionization on propagation and branching of positive and negative streamers in sprites. *Journal of Geophysical Research*, *109*(A4), A04301. https://doi.org/10.1029/2003JA010064

Lu, G., Jiang, R., Qie, X., Zhang, H., Sun, Z., Liu, M., et al. (2014). Burst of intracloud current pulses during the initial continuous current in a rocket-triggered lightning flash. *Geophysical Research Letters*, *41*(24), 9147–9181. https://doi.org/10.1002/2014GL062127

Lu, G., Zhang, H., Jiang, R., Fan, Y., Qie, X., Liu, M., et al. (2016). Characterization of initial current pulses in negative rocket-triggered lightning with sensitive magnetic sensor. *Radio Science*, *51*(9), 1432–1444. https://doi.org/10.1002/2016RS005945

Luque, A., & Ebert, U. (2014). Growing discharge trees with self-consistent charge transport: The collective dynamics of streamers. *New Journal of Physics*, *16*(1), 013039. https://doi.org/10.1088/1367-2630/16/1/013039

Mansell, E. R., MacGorman, D. R., Ziegler, C. L., & Straka, J. M. (2002). Simulated three-dimensional branched lightning in a numerical thunderstorm model. *Journal of Geophysical Research*, *107*(D9). ACL 2-1–ACL 2-12. https://doi.org/10.1029/2000JD000244

Mazur, V., & Ruhnke, L. H. (1998). Model of electric charges in thunderstorms and associated lightning. *Journal of Geophysical Research*, *103*(D18), 23299–23308. https://doi.org/10.1029/98JD02120

Naghizadeh-Kashani, Y., Cressault, Y., & Gleizes, A. (2002). Net emission coefficient of air thermal plasmas. *Journal of Physics D: Applied Physics*, *35*(22), 2925–2934. https://doi.org/10.1088/0022-3727/35/22/306

Nijdam, S., Teunissen, J., & Ebert, U. (2020). The physics of streamer discharge phenomena. *Plasma Sources Science and Technology*, *29*(10), 103001. https://doi.org/10.1088/1361-6595/abaa05

Pantuso, J., & da Silva, C. (2024). Simulation data used in "Modeling the Inception and Stepped Propagation of Positive Lightning Leaders" [Dataset]. *Zenodo*. https://doi.org/10.5281/zenodo.11176270

Pasko, V. P. (2014). Electrostatic modeling of intracloud stepped leader electric fields and mechanisms of terrestrial gamma ray flashes. *Geophysical Research Letters*, *41*(1), 179–185. https://doi.org/10.1002/2013GL058983

Popov, N. A. (2003). Formation and development of a leader channel in air. *Plasma Physics Reports*, *29*(8), 695–708. https://doi.org/10.1134/1.1601648

Pu, Y., Jiang, R., Qie, X., Liu, M., Zhang, H., Fan, Y., & Wu, X. (2017). Upward negative leaders in positive triggered lightning: Stepping and branching in the initial stage. *Geophysical Research Letters*, *44*(13), 7029–7035. https://doi.org/10.1002/2017GL074228

Qie, X., Jiang, R., Wang, C., Yang, J., Wang, J., & Liu, D. (2011). Simultaneously measured current, luminosity, and electric field pulses in a rocket-triggered lightning flash. *Journal of Geophysical Research*, *116*(D10), D10102. https://doi.org/10.1029/2010JD015331

Qie, X., Pu, Y., Jiang, R., Sun, Z., Liu, M., Zhang, H., et al. (2017). Bidirectional leader development in a preexisting channel as observed in rocket-triggered lightning flashes. *Journal of Geophysical Research: Atmospheres*, *122*(2), 586–599. https://doi.org/10.1002/2016JD025224

Qin, J., & Pasko, V. P. (2014). On the propagation of streamers in electrical discharges. *Journal of Physics D: Applied Physics*, *47*(43), 435202. https://doi.org/10.1088/0022-3727/47/43/435202

Rakov, V. A. (1998). Some inferences on the propagation mechanisms of dart leaders and return strokes. *Journal of Geophysical Research*, *103*(D2), 1879–1887. https://doi.org/10.1029/97JD03116

Rakov, V. A., Crawford, D. E., Kodali, V., Idone, V. P., Uman, M. A., Schnetzer, G. H., & Rambo, K. J. (2003). Cutoff and reestablishment of current in rocket-triggered lightning. *Journal of Geophysical Research*, *108*(D23), 4747. https://doi.org/10.1029/2003JD003694

Rakov, V. A., & Uman, M. A. (2003). *Lightning: Physics and effects*. University Press.

Riousset, J. A., Pasko, V. P., Krehbiel, P. R., Thomas, R. J., & Rison, W. (2007). Three-dimensional fractal modeling of intracloud lightning discharge in a New Mexico thunderstorm and comparison with lightning mapping observations. *Journal of Geophysical Research*, *112*(D15), D15203. https://doi.org/10.1029/2006JD007621

Rizk, F. (1994). Modeling of lightning incidence to tall structures, Part I + II. *IEEE Transactions on Power Delivery*, *9*, 162–193.

Saba, M. F., da Silva, R., Pantuso, J., & da Silva, C. L. (2022). Close view of the lightning attachment process unveils the streamer zone fine structure. *Geophysical Research Letters*, *49*(24). https://doi.org/10.1029/2022gl101482

Schumann, C., Saba, M. M. F., Warner, T. A., Ferro, M. A. S., Helsdon, J. H., Thomas, R., & Orville, R. E. (2019). On the triggering mechanisms of upward lightning. *Scientific Reports*, *9*(1), 9576. https://doi.org/10.1038/s41598-019-46122-x

Stenbaek-Nielsen, H. C., Kanmae, T., McHarg, M. G., & Haaland, R. (2013). High-speed observations of sprite streamers. *Surveys in Geophysics*, *34*(6), 769–795. https://doi.org/10.1007/s10712-013-9224-4

Syssoev, A. A., & Iudin, D. I. (2023). Numerical simulation of electric field distribution inside streamer zones of positive and negative lightning leader. *Atmospheric Research*, *295*, 107021. https://doi.org/10.1016/j.atmosres.2023.107021

Syssoev, A. A., Iudin, D. I., Bulatov, A., & Rakov, V. A. (2020). Numerical simulation of stepping and branching processes in negative lightning leaders. *Journal of Geophysical Research: Atmospheres*, *125*(7), 1–28. https://doi.org/10.1029/2019JD031360

Taylor, M. C., da Silva, C. L., Walker, T. D., & Christian, H. J. (2022). Data-constrained simulations of the lightning return stroke channel properties. *IEEE Transactions on Electromagnetic Compatibility*, *64*(5), 1461–1469. https://doi.org/10.1109/TEMC.2022.3189590

Wang, Z., Lu, G., Li, X., Fan, Y., Ren, H., Zhang, C., et al. (2023). Low frequency magnetic field observations of natural positive leaders featuring stepwise propagation. *Geophysical Research Letters*, *50*(20), e2023GL105540. https://doi.org/10.1029/2023GL105540

Wang, Z., Qie, X., Jiang, R., Wang, C., Lu, G., Sun, Z., et al. (2016). High-speed video observation of stepwise propagation of a natural upward positive leader. *Journal of Geophysical Research: Atmospheres*, *121*(24), 14307–14315. https://doi.org/10.1002/2016JD025605

Winn, W. P., Eastvedt, E. M., Trueblood, J. J., Eack, K. B., Edens, H. E., Aulich, G. D., et al. (2012). Luminous pulses during triggered lightning. *Journal of Geophysical Research*, *117*(D10), D10204. https://doi.org/10.1029/2011JD017105

Winn, W. P., Trueblood, J. J., Eack, K. B., Edens, H. E., Eastvedt, E. M., Aulich, G. D., et al. (2021). Triggered negative lightning-leaders that propagated into thunderstorm lower positive charge. *Journal of Geophysical Research: Atmospheres*, *126*(24), e2021JD034938. https://doi.org/10.1029/2021JD034938

Yoshida, S., Biagi, C. J., Rakov, V. A., Hill, J. D., Stapleton, M. V., Jordan, D. M., et al. (2010). Three-dimensional imaging of upward positive leaders in triggered lightning using VHF broadband digital interferometers. *Geophysical Research Letters*, *37*(5), L05805. https://doi.org/10.1029/2009GL042065